



Research Paper

CFD Investigations on a Plate-and-Frame Forward Osmosis Module: Effects of Novel System Parameters

Shivang Rampriyan, Bahni Ray*

Department of Mechanical Engineering, Indian Institute of Technology Delhi, New Delhi 110016, India

Article info

Received 2023-04-03

Revised 2023-07-10

Accepted 2023-08-18

Available online 2023-08-18

Keywords

Forward osmosis
Concentration polarization
Computational fluid dynamics
Parametric studies
Module-scale modeling
Porous media flow

Highlights

- Ratios of inlet concentrations and speeds used for performance assessment.
- A case-invariant optimal range for pure water permeability of support was proposed.
- An index for the efficient modeling of fluid flow in membrane support was defined.

Abstract

We undertake a two-dimensional computational fluid dynamics (CFD) study to evaluate the performance of a plate-and-frame forward osmosis (FO) module. The performance was primarily quantified by the transmembrane water flux. We used the ratios of inlet concentrations and speeds to conduct parametric assessments on the module. The base case was tested for flux consistency with co-current and countercurrent configurations. The influence of the support's pure water permeability (κ) on water flux was assessed, and an optimal range for κ -sensitivity (ORKS) was proposed. The ORKS was found to be a configuration-invariant performance control parameter for FO system performance and is critical to preventing overdesign situations. We conclude by suggesting a membrane modeling index, S^* , which can be compared to the conventional membrane structural parameter, S , to make informed decisions about the physical model that could be used to model fluid flow inside the porous support.

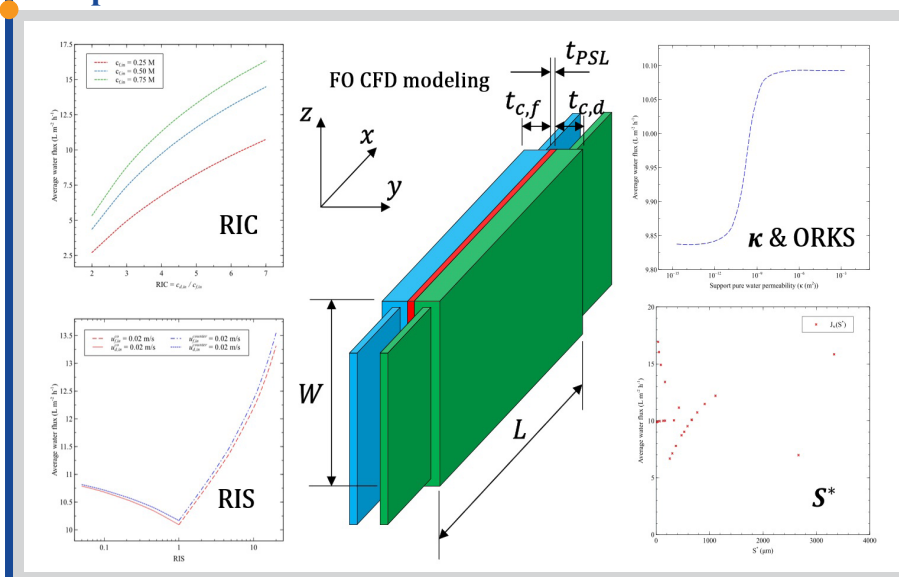
© 2023 FIMTEC & MPRL. All rights reserved.

1. Introduction

Based on the orientation of the asymmetric hydrophilic membrane (feed or draw facing selective layer), Forward Osmosis (FO) and Pressure-retarded Osmosis (PRO) are two popular osmotically driven membrane processes (ODMPs) [1]. While the former is usually used as a separation process, the latter tends to find applications in osmotic energy generation [1]. Unlike conventional membrane processes like Reverse Osmosis (RO), Nano-/Ultrafiltration (NF/UF), FO does not require any external hydraulic pressure to function and is wholly driven by the natural osmotic pressure difference ($\Delta\Pi$) between the feed and the draw solutions, which makes it

a low-energy process [2]. Due to low hydraulic pressure gradients in FO, contaminant compaction on the membrane surfaces is minimal, which ensures that most observed fouling in FO systems is reversible [3]. This is unlike RO and NF/UF systems, which are pressure-driven and experience irreversible fouling on the surfaces of their membranes. Another key advantage of FO systems over conventional membrane-based technologies is the high selectivity of their membranes, which arises due to the reverse draw solute flux hindering feed solute(s) forward diffusion through the membrane pores [4]. Since experimental investigations are limited by apparatus cost and testing

Graphical abstract



* Corresponding author: bray@iitd.ac.in(B. Ray)

complexities, numerous modeling studies have been proposed to better understand the performance of FO systems for varied ranges of system parameters [5–8].

The water flux obtained in FO systems is far less than expected based on the bulk $\Delta\Pi$ between the feed and the draw solutions. A large fraction of the bulk $\Delta\Pi$ is lost due to concentration polarization (CP) effects in the module (internal CP (ICP) in the porous support, external CP on the membrane interfaces). While primitive models conveniently neglect CP phenomena [9], contemporary models comprehensively incorporate the effects of CP phenomena on module performance [10]. McCutcheon and Elimelech [11] proposed a 1D solution-diffusion model that calculated the transmembrane water flux by considering ICP in the membrane and ECP on the selective layer-feed interface. They, however, neglected the reverse draw solute (RDS) flux and draw side ECP, where the latter was shown to have appreciable effects on FO performance, especially at lower flow rates [7]. Phillip et al. [12] improved upon the extant models by incorporating RDS flux in their calculations but still ignored ECP in the module. Suh and Lee (2013) provided a reasonably comprehensive 1D mass transfer model for the FO process, which was able to simulate the effects of feed and draw ECP, RDS flux, and membrane ICP on the water flux. Attarde et al. [13] analyzed FO systems using the three-parameter Spiegler-Kedem model, which uses a reflection coefficient as a correction factor for the non-ideality of the FO membrane. However, their study was focused on spiral-wound module configuration and investigated FO performance for a limited range of system parameters. In a similar study, Sekino [14] used irreversible thermodynamics in addition to the Spiegler-Kedem equation to propose a bilayer support model for a hollow fiber FO module which models for the convective solute flux in addition to the diffusive salt flux.

Recently, modeling investigations have started leveraging the powerful capabilities of computational fluid dynamics (CFD) to better understand the mass transfer phenomena in FO systems [5–8,15]. As discussed earlier, CP is an important phenomenon associated with FO systems. CFD helps quantify CP without altering the bulk flow by inserting probes and measurement devices [16]. Often, FO modules have complicated geometries and flow patterns. Full-scale simulations using CFD offer users an unprecedented opportunity to study the effects of flow hydrodynamics on mass transfer. Spacers are inherent to spiral-wound FO modules. It is challenging to analyze the effects of spacers on the flow and mass transfer characteristics of such modules. CFD not only helps predict the performance of spacer-embedded spiral-wound FO modules but also helps test and optimize novel spacer designs and configurations without requiring long and expensive experimentation [17–19].

Using CFD, Pozzobon & Perré [20] resolved fluid flow around the fibers in a hollow fiber membrane contactor and determined the shell side resistance. Binger & Achilli [21] performed several hundred CFD simulations of spacer-filled membrane channels and produced models to predict pressure drop and mass transfer coefficients. They also integrated high-fidelity data generated from CFD with machine learning optimization algorithms, which illustrates the implementation flexibility CFD simulations offer. Bae et al. [22] performed a 3D CFD study on the effects of woven and non-woven RO feed spacers on mitigating feed-side CP and suggested efficient spacer designs and flow patterns. Yang et al. [23] performed CFD investigations on a seawater RO desalination system and proposed a multiscale modeling approach using different wall boundary conditions. Using CFD for simulating mass transfer in spacer-filled RO channels helped them resolve the flow to sub-millimeter scale details while providing opportunities to upscale the results to the systemscale. Chong et al. [24] performed 3D CFD simulations on a membrane channel with several twisted feed spacer configurations. They visualized the flow features and concluded that twisted spacers promote vortex generation and minimize stagnant zones. This indicates that CFD is an efficient tool to visualize and identify flow phenomena.

Often, there is a significant difference in the magnitudes of the feed and draw inlet concentrations. To quantify their relative imbalance within a single metric, we define the ratio of inlet concentrations (RIC) as an independent parameter in our study and use it for performance evaluation. Flow rate ratio (ratio of feed and draw solution flow rates) is a parameter that has been used in a few 1D-modeling studies to evaluate and optimize FO module performance [25]. However, through our literature survey, we could not find any CFD study that investigates FO performance using flow rate ratios. Due to reasons discussed in section 3.3, we use the ratio of inlet speeds (RIS) instead of flow rate ratios to conduct our analysis. Although several works have studied the influence of membrane parameters on FO performance, we found no study that explored the effects of the support layer pure water permeability (κ) on FO module performance. In this pursuit, we define an optimal range of κ -sensitivity (ORKS), a configuration-invariant module parameter that helps to select the best κ values for efficient FO operation.

The ORKS becomes increasingly crucial in FO system design as the draw solute concentration is increased (see section 3.4).

CFD investigations on FO systems often use the Brinkman Equation to model fluid flow inside the membrane [5,6,8]. Solving the weakly compressible form of the Brinkman Equation (see section 2.2) is computationally expensive and rarely needed because the Brinkman Equation often reduces to Darcy's Equation or a Navier-Stokes form with a modified viscosity for a specific combination of membrane parameters. There is no well-defined paradigm with which one could ascertain the relevance of the Brinkman Equation in a particular modeling situation. To address this limitation, we introduce a novel membrane modeling index for accelerated convergence (S^*), which when compared to the conventional membrane structural parameter (S), yields useful insights on the type of governing equation to be used for membrane fluid flow modeling for reducing the solution time. For example, Sagiv et al. [8] have simply used the Brinkman Equation for modeling fluid flow inside their FO membrane. However, for the membrane parameters provided in their paper, $S^* \ll S$ (see section 3.6 for details), the Brinkman Equation could have been replaced by Darcy's Equation, which would then reduce the solution time significantly without compromising solution accuracy.

In this paper, we developed a 2D finite element numerical model for evaluating the performance of a plate-and-frame FO module, which we measure by calculating the transmembrane water flux in the module. We validate our results with experimental data provided in [12] and compare our results with a 1D model and an existing CFD model given by Kahrizi et al. [5]. We then simulate our model for various system parameters and explore the effects of RIC, RIS, and membrane support layer properties on module performance. We introduce a novel configuration-invariant module parameter for support permeability, ORKS, and a membrane modeling index, S^* , which yields crucial insights into solution times when compared to the conventional membrane structural parameter, S .

2. Model Development

We developed a validated finite element numerical model for assessing the performance of a two-channelled plate-and-frame FO module. The 3-D module design, as prescribed in Phillip et al. [12] and illustrated in Fig. 1, was simplified into a 2-D geometry for ease of analysis, which was possible due to the conspicuous existence of x-y symmetry planes along the width of the module. We consider both the feed and the draw solutions to be mono-species aqueous solutions with varying NaCl concentrations. Our model can capture the ICP effect in the support layer and ECP on both sides of the membrane. It can also calculate the local RDS flux in the system alongside the usual transmembrane water flux.

The basic workflow for our model's development is briefed here. We start with a description of the model geometry, list the governing equations and boundary conditions for the FO process, define the study parameters, variables, and properties, and provide the methodology for numerical analysis of our problem. The following subsections elucidate these procedures in detail.

2.1. Model geometry, simplifications, and assumptions

The original design (see Fig. 1) consisted of two channels created due to the separation of two flat plates with a membrane. Enclosed by flat plates, one channel carries the feed solution, and the other carries the draw solution. The flat plates were approximated as linear boundaries, while the fluid flow and membrane domains were modeled as rectangular domains in our study. The lengths of the channels for fluid flow, and the length of the membrane, are all equal L . The width of the feed channel is indicated by $t_{c,f}$ and that of the draw channel by $t_{c,d}$. The selective layer of a hydrophilic FO membrane being at most a few nanometres thick (~40-300 nm, see Yip & Elimelech [26] for details), we ignore its thickness in comparison to the much thicker support layer, whose thickness is typically in the order of a few dozen micrometers (~50-100 μm , see Yip et al. [27] for details). This saves us valuable computational time and resources due to a reduction in the required mesh size for the bilayer membrane. The support layer thickness is represented by t_{PSL} . The entire model geometry is illustrated in Fig. 2. To further simplify the modeling procedure, the following assumptions were introduced in the study:

1. Steady-state operating conditions.
2. Weakly compressible (constant reference pressure) laminar flow in the feed and the draw channels.

3. The no-slip boundary condition at the channel plates.
4. No velocity and concentration discontinuities at the support layer-draw channel interface.
5. The membrane has a homogeneous pore structure with constant intrinsic properties like permeability, porosity, and tortuosity.

2.2. Governing equations and boundary conditions

Laminar flow in the feed and draw channels is modeled using the weakly compressible form of the Navier-Stokes equations, where fluid properties of the aqueous solutions, like dynamic viscosity and density, may vary with solute concentration but are calculated at a constant reference pressure (1 atm in our case). A similar approach has been adopted in several other CFD studies on FO [5,7,8]. The solute concentration distribution in the membrane support, feed, and draw channels was modeled using the advection-diffusion equation with solute concentration as the dependent variable. The flow inside the membrane support was described using the Brinkman equation. The equations were extensively coupled and solved simultaneously. More details about the governing equations are provided in the subsequent subsections.

2.2.1. Momentum transport

We first calculate the hydraulic diameter of the channels to ensure that the fluid velocities we consider in our study are appropriate for considering laminar velocity fields in the channels. The hydraulic diameter, D_h , of a channel is given as,

$$D_h = \frac{2Wt_{c,i}}{W + t_{c,i}} \quad (1)$$

where W is the channel width in the z-direction, $t_{c,i}$ is the channel thickness as illustrated in Fig. 1, with i representing f or d , for the feed and the draw, respectively. Since $W > 10t_{c,i}$ Eq. (1) can be approximated as,

$$D_h \cong 2t_{c,i} \quad (2)$$

We use Eq. (2) in obtaining the Reynolds' Number, Re , as $Re_{D_h} = \frac{\bar{u}D_h}{\nu}$. To avoid the onset of turbulence in the channels, the maximum \bar{u} we consider is 0.4 m/s, which yields $Re_{D_h} \sim 2100$ for the

base case (see section 2.3.3 for further details). Therefore, the weakly compressible laminar form of the Navier-Stokes equations, along with the continuity equation, may be used for modeling the hydrodynamics of the channels [7]. For the feed and draw channels, the governing equations become [7],

$$\frac{\partial(\rho_i u_i)}{\partial x} + \frac{\partial(\rho_i v_i)}{\partial y} = 0 \quad (3)$$

$$\left(u_i \frac{\partial u_i}{\partial x} + v_i \frac{\partial u_i}{\partial y} \right) = -\frac{1}{\rho_i} \frac{\partial P_i}{\partial x} + \frac{\mu_i}{\rho_i} \left(\frac{\partial^2 u_i}{\partial x^2} + \frac{\partial^2 u_i}{\partial y^2} \right) \quad (4)$$

$$\left(u_i \frac{\partial v_i}{\partial x} + v_i \frac{\partial v_i}{\partial y} \right) = -\frac{1}{\rho_i} \frac{\partial P_i}{\partial y} + \frac{\mu_i}{\rho_i} \left(\frac{\partial^2 v_i}{\partial x^2} + \frac{\partial^2 v_i}{\partial y^2} \right) \quad (5)$$

where i can be d or f for the draw and feed streams, respectively, and u_i, v_i are the x and y-components of the fluid velocity in the channels (u_i), P_i is the hydrodynamic pressure, and μ_i and ρ_i are the dynamic viscosity and density of the solution, respectively.

For the membrane support, we use the Brinkman equation [8],

$$-\frac{\partial P_m}{\partial x} + \frac{\mu_d}{\varepsilon} \left(\frac{\partial^2 u_m}{\partial x^2} + \frac{\partial^2 u_m}{\partial y^2} \right) = u_m \frac{\mu_d}{\kappa} + \frac{\rho}{\varepsilon^2} \left(u \frac{\partial u_m}{\partial x} + v \frac{\partial u_m}{\partial y} \right) \quad (6)$$

$$-\frac{\partial P_m}{\partial y} + \frac{\mu_d}{\varepsilon} \left(\frac{\partial^2 v_m}{\partial x^2} + \frac{\partial^2 v_m}{\partial y^2} \right) = v_m \frac{\mu_d}{\kappa} + \frac{\rho}{\varepsilon^2} \left(u \frac{\partial v_m}{\partial x} + v \frac{\partial v_m}{\partial y} \right) \quad (7)$$

where ε is the porosity, κ is the permeability of the porous support, u_m, v_m are the x and y-components of the fluid velocity inside the membrane (u_m).

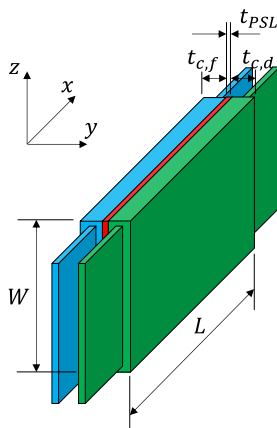


Fig. 1. Original design of the FO module (reconstructed from the description provided by Phillip et al. (2010)). $W=26$ mm, $L=77$ mm, $t_{c,f}=t_{c,d}=3$ mm, $t_{psl}=50\mu\text{m}$.

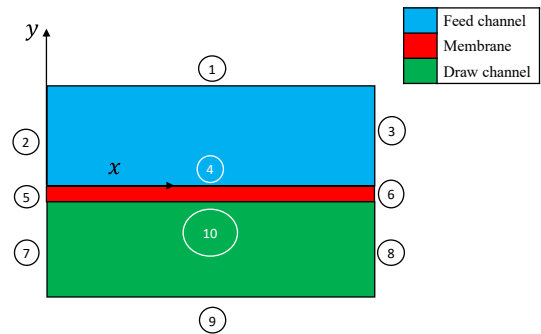


Fig. 2. Simplified model geometry for numerical analysis. The circled numbers indicate the boundary number.

2.2.2. Solute transport

Both the feed and draw solutions are aqueous salt solutions. Besides solute diffusion, the flow fields in the channels induce bulk advection of the solute. Assuming no relative slipping between the solute and the water

molecules, the solute transport in the channels is governed by the advection-diffusion equations [6],

$$\frac{\partial}{\partial x} \left(-D_i \frac{\partial c_i}{\partial x} + c_i u_i \right) + \frac{\partial}{\partial y} \left(-D_i \frac{\partial c_i}{\partial y} + c_i v_i \right) = 0 \quad (8)$$

where i can be d or f for the draw and feed streams, respectively, and u_i, v_i are the x and y-components of the solution velocity u_i , D_i is the bulk diffusion coefficient of the solute in water, and c_i is the solute concentration.

Inside the membrane support layer, Eq. 8 becomes [9],

$$\frac{\partial}{\partial x} \left(-D_d \frac{\varepsilon}{\tau} \frac{\partial c_m}{\partial x} + c_m u_m \right) + \frac{\partial}{\partial y} \left(-D_d \frac{\varepsilon}{\tau} \frac{\partial c_m}{\partial y} + c_m v_m \right) = 0 \quad (9)$$

where τ is the tortuosity and c_m is the solute concentration inside the porous support, and other symbols have their usual meanings.

2.2.3. Osmosis-driven water flux

The transmembrane water flux, J_w , is generated due to the osmotic pressure difference ($\Delta\Pi$) between the feed and the draw solutions on either side of the membrane. In FO modules J_w can be expressed as,

$$J_w = A(\Pi_i - \Pi_{f,m}) \quad (10)$$

where A is the pure water permeability of the selective layer, Π_i is the osmotic pressure of the draw solution at the interface of the selective layer and the porous support layer, and $\Pi_{f,m}$ is the osmotic pressure of the feed solution at the feed-membrane interface. Since J_w is different at each point along the length of the membrane, we use the line-averaged form, $\overline{J_w}$, to refer to the average water flux in the module.

Similarly, the RDS flux in FO modules can be written as,

$$J_s = B(c_i - c_{f,m}) \quad (11)$$

where B is the draw solute permeability of the selective layer, c_i is the draw solute concentration at the interface of the selective layer and the porous support layer, and $c_{f,m}$ is the concentration of the feed solution at the feed-membrane interface.

The $\overline{J_w}$ obtained through our CFD study is compared with the value obtained using the 1D solute-diffusion model, which includes all CP phenomena. From the 1D model, J_w ($=\overline{J_w}$) is given as [28],

$$J_w = A \left[\frac{\Pi_{db} \exp \left[1 - J_w \left(\frac{1}{k_d} - \frac{S}{D_d} \right) \right] - \Pi_{fb} \exp \left(\frac{J_w}{k_f} \right)}{1 + \frac{B}{J_w} \left[\exp \left(\frac{J_w}{k_f} \right) - J_w \left(\frac{1}{k_d} - \frac{S}{D_d} \right) \right]} \right] \quad (12)$$

where π_{db} is the bulk draw solution Π , k_i is the mass transfer coefficient for water transport between the membrane and i (i is f or d for the feed and draw, respectively), and S is the membrane structural parameter.

2.2.4. Boundary conditions

The boundary conditions (BCs) used while solving the governing equations enumerated in Eqs. 3-9 are described in Table 1. Since the co-current configuration is the dominant flow configuration in this study, the BCs in Table 1 are for the same configuration. For the countercurrent configuration, we can exchange the conditions at the inlet and outlet of one of the channels.

Table 1
Boundary conditions for the simplified module design illustrated in Fig. 2

Boundary	MT-feed	MT-membrane	MT-draw	ST-feed	ST-membrane	ST-draw
1	$u_f = v_f = 0$			$-D_f \frac{\partial c_f}{\partial y} = 0$		
2	$u_f = u_{f,in}$, $v_f = 0$			$c_f = c_{f,in}$		
3	$P_f = P_{atm}$			$-D_f \frac{\partial c_f}{\partial x} = 0$		
4	$u_f = 0$, $v_f = -J_w$	$u_m = 0, v_m = -J_w$		$-D_f \frac{\partial c_f}{\partial y} = J_s$	$-D_d \frac{\varepsilon}{\tau} \frac{\partial c_m}{\partial y} = J_s$	
5		$u_m = v_m = 0$			$-D_d \frac{\varepsilon}{\tau} \frac{\partial c_m}{\partial x} = 0$	
6		$u_m = v_m = 0$			$-D_d \frac{\varepsilon}{\tau} \frac{\partial c_m}{\partial x} = 0$	
7			$u_d = u_{d,in}$, $v_d = 0$			$c_d = c_{d,in}$
8			$P_d = P_{atm}$			$-D_d \frac{\partial c_d}{\partial x} = 0$
9			$u_d = v_d = 0$			$-D_d \frac{\partial c_d}{\partial y} = 0$
10		$u_m = u_d, v_m = v_d$, $\tau_{yx} _m = \tau_{yx} _d$, $P_m = P_d$	$u_d = 0$, $v_d = -J_w$		$c_m = c_d$	$-D_d \frac{\partial c_d}{\partial y} = J_s$

MT: Momentum transport, ST: Solute transport

2.3. Defining solution properties, system parameters, and operating conditions

The model simulations investigate the FO process for a diverse set of parameters and their ranges. Similarly, the module performance is tested for multiple operating configurations and solutes. The following subsections describe these details.

2.3.1. Solution properties

An aqueous solution of NaCl has been used for the simulations as feed and draw solutions. The corresponding thermophysical properties and osmotic pressure as functions of solute concentration at room temperature (298.15 K) are summarized in Table 2. The properties were extracted from OLI Stream Analyzer v3.1.3 (OLI Systems, Inc.) and fitted into polynomial functions.

2.3.2. System parameters and operating conditions

Since we intend to investigate the effects of changing system parameters on module performance, we consider one configuration as the base case and vary the system parameters accordingly. The system control parameters can be divided into two categories—design parameters (concerning module geometry and operating conditions) and membrane parameters. Table 3 enlists all such parameters with their respective classification.

2.4. Meshing and grid independence

Considering the simplicity of the geometry, we used a structured mesh to discretize our governing equations and solve the numerical model. The mesh is composed of rectangular elements, as shown in Fig. 3. We use finer mesh near the model boundaries, inlets, and outlets, to resolve sharper boundary gradients. To achieve this, the maximum mesh element dimension was taken as 271 μm, while 12.2 μm was kept the minimum. The maximum growth rate of an element was fixed at 1.2. A linear growth rate of 5 was selected for a symmetric y-direction discretization of the fluid domains, while identically sized elements were used for discretizing the membrane in the y-direction. An exponential growth rate of 3 was selected for the x-direction discretization of all domains.

We implemented a grid convergence study to ensure that the mesh we use in our study is optimal. By varying the total number of mesh elements, as illustrated in Fig. 4, we observe that a stable value of water flux, $\overline{J_w}$, was obtained for a total mesh number of 22200. At this discretization level, we also observe that the aspect ratio of each element is good enough for obtaining mesh-independent solutions. The total mesh number will change as we vary the geometry of our model. Appropriate mesh adaptations have been introduced in our model to cater to the geometry changes. We use a structured mesh in our simulations to ensure that the change in geometry does not distort the meshing quality.

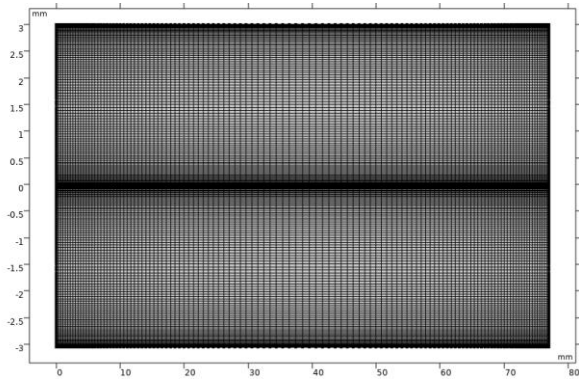


Fig. 3. A structured mesh was used to discretize the model. The base case was discretized into 22200 elements (Figure scaled to fit the window for visual clarity).

Table 2
Thermophysical properties and osmotic pressures of aqueous NaCl solution at 298.15 K (c in M)

Property (symbol, unit)	Function
Density (ρ , kg / m^3)	$995.7 + 39.92c - 1.235c^2$
Dynamic viscosity (μ , $Pa - s$)	$7.98 \times 10^{-4} + 7.53 \times 10^{-5}c + 1.037 \times 10^{-5}c^2 - 8.81 \times 10^{-8}c^3$
Diffusivity (D, m^2 / s)	$1.71 \times 10^{-9} (1 - 1.099c + 8.129c^2 - 31.6c^3 + 57.5c^4 - 39.4c^5), c \in [0, 0.5M]$
Osmotic pressure (Π , bar)	$1.71 \times 10^{-9} (1 - 0.0778c + 0.0039c^2), c \in [0.5M, 4.5M]$
Osmotic pressure (Π , bar)	$9.5508c^2 + 32.895c + 0.5081$

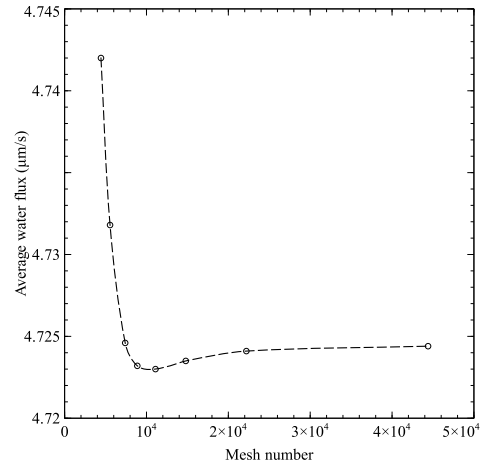


Fig. 4. Testing for grid independence by monitoring the variation in $\overline{J_w}$ with a changing mesh size. $c_{f,in} = 0M$ (DI feed), $c_{d,in} = 3M$, $u_{f,in} = u_{d,in} = u^v = 0.214 m / s$, $A = 1.23 \times 10^{-12} m^2 - s / kg$, $B = 7.25 \times 10^{-8} m / s$, $\epsilon = 0.2$, $\tau = 1.5$.

2.5 Numerical paradigm

We followed a stepwise approach to obtain rapidly converging and bounded solutions to our equations. We used quadratic and linear shape functions to interpolate the velocity and pressure, respectively, between a pair of element nodes. Also, we employed quadratic shape functions for concentration interpolation between element nodes to obtain a well-resolved concentration distribution in the membrane.

While solving the system of equations for the base case, we first solved an incompressible formulation of laminar flow in the feed channel by assuming reasonable values of water and reverse solute fluxes. Our assumed values were inspired by several experimental FO studies [12,27,29]. The calculated velocity field was inserted in Eq. 8 to obtain the concentration distribution of solute in the feed channel. The assumed fluxes were then used to obtain the velocity field and solute concentration distribution in the draw solution and membrane domains. Once the solute concentration throughout the module was obtained, we solved for the velocity field in the feed, membrane, and draw domains using the weakly compressible formulation of the Navier-Stokeequations, as outlined in section 2.2.1. The advection-diffusion equations for obtaining a solute concentration in the module were simultaneously solved with the velocity field, alongside the water and reverse solute flux, to ensure a rigorous physical coupling. All initial values were obtained from the previous solution set (based on the assumed fluxes), ensuring faster convergence for the coupled solutions. All implementations were performed using COMSOL Multiphysics 6.0 on a PC with a 5.0 GHz (after boost) 16-core Intel i5 12th generation processor, 16 GB DDR5 RAM, and 4 GB Nvidia GeForce RTX3050i GPU. The simulation time ranged from a few minutes to an hour, depending on the type of parametric study undertaken. The simplest base case took 3 minutes and 52 seconds to run. Parametric studies took significantly more time. For example, simulations performed with a changing RIS took 16 minutes and 8 seconds to complete. Parametric studies that involved a change in the geometrical dimensions of the module took even longer to conclude. The entire process is summarized in Fig. 5.

Table 3
System parameters—design, operation, and membrane. The value of a specific parameter in the base configuration is given in underlined boldface font.

Category	Parameter name (unit)	Symbol	Value(s)	
Design parameters	Module length (mm)	L	<u>77</u>	
	Module geometry	Feed channel thickness (mm)	$t_{c,f}$	1.5, 2.25, <u>3</u> , 3.75, 4.5, 5.25, 6
		channel thickness (mm)	$t_{c,d}$	1.5, 2.25, <u>3</u> , 3.75, 4.5, 5.25, 6
	Operating configuration	Feed inlet speed (m/s)	$u_{f,in}$	<u>0.02</u> , 0.04, 0.06, 0.08, 0.10, 0.20, 0.214 ^v , 0.30, 0.40
		aw inlet speed (m/s)	$u_{d,in}$	<u>0.02</u> , 0.04, 0.06, 0.08, 0.10, 0.20, 0.214 ^v , 0.30, 0.40
		Feed inlet solute concentration (M)	$c_{f,in}$	0.25, <u>0.50</u> , 0.75
Draw inlet solute concentration (M)		$c_{d,in}$	1.0, 1.5, 2.0, 2.5, <u>3.0</u> , 3.5, 4.0, 4.5	
Membrane parameters	Selective layer	Pure water permeability (m ² -s/kg)	A	<u>1.23×10^{-12}</u>
		Solute permeability (m/s)	B	<u>7.25×10^{-8}</u>
	Porous support layer	Porosity	ϵ	[0.10, 0.85](<u>0.20</u>) ^b
		Tortuosity	τ	[1.10, 1.90](<u>1.50</u>) ^b
		Thickness (μm)	t_{PSL}	[10, 130](<u>50</u>) ^b
		Pure water permeability (m ²)	κ	$[2 \times 10^{-15}, 2 \times 10^{-3}](2 \times 10^{-9})$ ^b

^v: value used for validation

^b: The simulations are performed for several random parameter values within the given interval, and the base value is given in parentheses.

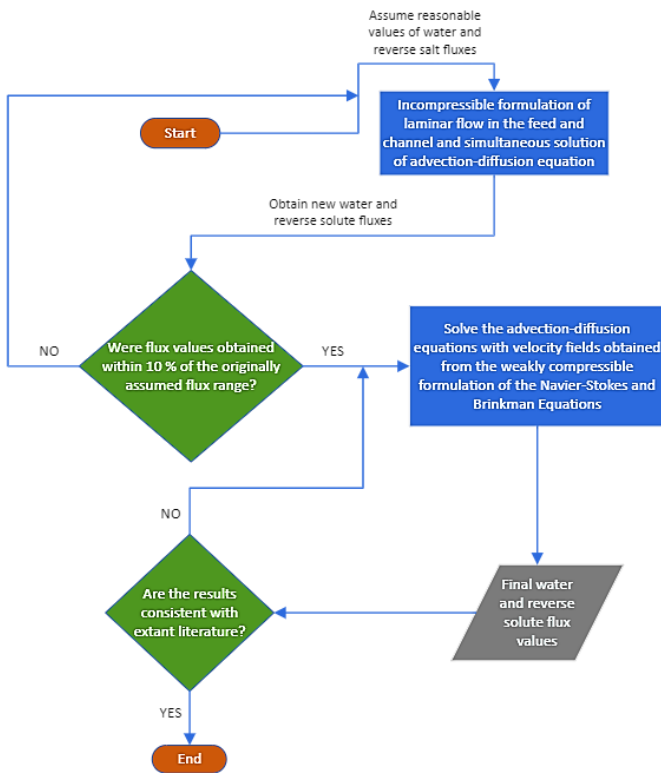


Fig. 5. Flowchart for the methodology followed while solving the governing equations associated with the current study.

2.6 Introducing a membrane modeling index for physics-driven computational efficiency

Let us consider solving for the flow field of a water-filled, porous rectangular domain of width t_{PSL} and length L . The domain properties like porosity, tortuosity, and pure water permeability are identical to that of the membrane support layer for the base case in our study. The operating flow parameters and the numerical methodology are identical to the base case. We take a grid size of 300×80 (300 elements along the length and 80 elements along the width with a symmetric and linear growth ratio of 6 for both dimensions). Table 4 indicates the solution time required for solving the flow

field in the domain using each of the Darcy, Laminar, and Brinkman flow configurations. We note that the solution time is in the order $t_{Darcy} < t_{Laminar} < t_{Brinkman}$. A similar trend in solution times is observed when the porous support layer is simulated along with the entire FO module (not demonstrated here). Therefore, the computational costs involved in modeling FO modules may be significantly reduced if we use the Laminar or Darcy flow equations instead of the Brinkman equation to model fluid flow inside the support layer. Therefore, we define a membrane modeling index, S^* , to ascertain the need for the full-Brinkman type formulation in our model.

To obtain S^* , we non-dimensionalize Eq. 6 with the magnitude scales $x \sim L$, $y \sim t_{PSL}$, $v \sim J_w$, $u \sim \frac{J_w L}{t_{PSL} \tau}$ (from mass conservation), $P \sim \frac{1}{2} \rho \left(\frac{J_w^2 L^2}{t_{PSL}^2 \tau^2} \right)$ as,

$$u_i^\# \frac{\partial u_i^\#}{\partial x^\#} + v_i^\# \frac{\partial u_i^\#}{\partial y^\#} = -\frac{\epsilon^2}{2} \frac{\partial P_i^\#}{\partial x^\#} + \frac{v}{J_w} \left(-\frac{1}{S^*} u^\# + \frac{1}{S} \frac{\partial^2 u^\#}{\partial y^{\#2}} \right) \quad (13)$$

where $()^\#$ indicates the non-dimensional form of a variable, $S^* = \frac{\kappa}{t_{PSL} \tau \epsilon^2}$,

and $S = \frac{t_{PSL} \tau}{\epsilon}$. To form a general intuition about the modeling relevance of

S^* , we observe from Eq. 13 that S^* and S signify the relative importance of the Darcy and viscous terms, respectively. When $S^* \gg S$, we can say that the flow inside the membrane support layer is viscosity-driven and well-explained by the Navier-Stokes formulation of the velocity field in the membrane domain. In addition, due to the high permeability of the membrane, the flow can be approximated as that in a fluid-filled channel with modified fluid properties. This enables us to determine the appropriateness of a detailed consideration of the porous structure of the membrane support compared to approximating the membrane as a fluid. For cases where $S^* \ll S$, the flow in the membrane support is well-explained by the Darcian formulation of the fluid velocity field in the support layer.

Table 4
Solution times of the test case using three flow modeling equations

Flow equation used	Solution time with 300×80 elements (in s)
Darcy $\left(u = -\frac{\kappa}{\mu} \nabla P\right)$	2
Laminar $\left(\rho(u \cdot \nabla)u = \nabla \cdot (-PI + \mu \nabla^2 u)\right)$	4
inkman $\left(\frac{1}{\varepsilon^2} \rho(u \cdot \nabla)u = \nabla \cdot (-PI + \mu \nabla^2 u) - \frac{\mu}{\kappa} u\right)$	10

3. Results and discussion

The performance of the module was measured by monitoring J_w , which was calculated for each configuration designed in the study. While the impeding effects of RDS flux, J_s , on J_w have been considered in the physics of the modeling, we were disinclined to include J_s as a performance parameter. This is because a typical value of J_s ($kg / m^2 - s$) in our study has an order, $O(10^{-6})$, while J_w (usual unit converted to the $kg / m^2 - s$) ranges in $O(10^{-3})$. With these magnitudes, we found that J_s did not have a significant effect on feed concentration/draw dilution and successive reduction in $\Delta\Pi$. Therefore, we found J_w as a suitable performance indicator for all practical purposes enumerated in this study. In some long channel configurations, we also discuss the outlet concentrations of both the feed and the draw channels, $C_{i,out} |_{i=f,d}$.

3.1. Model validation

We validated our modeling results from the experimental study by Phillip et al. (2010). In addition, we also compared our investigation to the 1D model [28] and the CFD model by Kahrizi et al. (2020) to demonstrate the improvements achieved through our study. The results are presented in Fig. 6. The J_w predictions obtained through CFD modeling are in good agreement with experimental data. We also observe that the 1D model (see Eq. (12)) strays far from predicting accurate flux values, especially at higher concentrations ($>1.5M$). In fact, the error increases more than two-fold when increasing the draw solute concentration from $3M$ to $4M$. The 1D model is unable to obtain the distribution of water flux and other process parameters along the length of the membrane. It is also unable to incorporate the effects of the hydrodynamics of draw and feed channel flows on module performance. Clearly, for an effective module-scale understanding of the FO process, our CFD model outperforms 1D models.

Our model fit predicts the best in the range $[1M, 3M]$. Similar results have been obtained by Kahrizi et al. (2020), but their model constantly overpredicts \bar{J}_w when compared with experimental data. We obtain comparable results if we do not consider boundary slip at the porous support-draw interface. However, neglecting interfacial slip may have a significant impact on draw-side ECP when considering highly pervious and/or loosely packed supports [7,30]. When $c_{d,in}$ is increased beyond $4M$, we observe considerable deviations in the predicted \bar{J}_w values from experimental results. This is due to a reduced accuracy of software-predicted solution properties at higher solute concentrations.

3.2 Variation in \bar{J}_w with the ratio of inlet concentrations (RIC)

For an elaborate understanding of the effects of the relative difference between the feed and draw inlet solute concentrations, we define RIC as,

$$RIC = \frac{c_{d,in}}{c_{f,in}} \tag{14}$$

where $c_{d,in}$ and $c_{f,in}$ are the inlet solute concentrations of the draw and the feed streams, respectively. When exploring the effects of draw solute concentration on module performance, typical FO studies have focused on c_d [5,6] or the driving force, $\Delta\Pi$ [12,31]. In both cases, it is difficult to ascertain the effects of simultaneous changes in $c_{f,in}$ and $c_{d,in}$ on \bar{J}_w . RIC helps in overcoming this difficulty, as illustrated in Fig. 7. The objective has been to vary $c_{d,in}$ in the range $[0.5M, 5M]$, which is supported by several previous works [12,32,33]. We vary the feed inlet solute concentration, $c_{f,in}$ in steps of 0.25 M from 0.25 M to 0.75 M. As expected, \bar{J}_w increases with an increase in RIC. The effect is more pronounced for higher values of $c_{f,in}$ due to an increase in the feed-draw concentration difference, and subsequently, $\Delta\Pi$. From Fig. 7 we also observe that at a particular value of RIC, the water flux J_w as $c_{f,in}$ is increased, is compromised. Hence, while keeping the RIC constant, the best water flux benefits can be derived by increasing $c_{f,in}$ when it is on the lower side.

Another helpful insight that can be derived from Fig. 7 is the relative effects of changing $c_{f,in}$ and RIC. The flux is more sensitive to changes in $c_{d,in}$ when $c_{f,in}$ is low. For example, when the RIC is changed from 2 to 7, \bar{J}_w for $c_{f,in} = 0.25M$ increases by nearly 300 %, while that for $c_{f,in} = 0.75M$ increases only by 200 %. Fig. 7 also highlights a crucial conclusion concerning the sensitivity to change in \bar{J}_w upon changing the stream inlet concentrations. For a certain configuration with RIC=6 and $c_{f,in} = 0.75M$, we have $c_{d,in} = 4.5M$. $c_{d,in}$ may be reduced threefold by decreasing either the RIC or $c_{f,in}$ to one-third of its initial value. In the former case, \bar{J}_w decreases from 14.94 LMH to 5.34 LMH (~64 % decrease), while for the latter, it decreases from 14.94 LMH to 9.59 LMH (~36 % decrease). It is, therefore, clear that for an identical change in $c_{d,in}$, \bar{J}_w is more sensitive to changes in RIC than solely $c_{f,in}$.

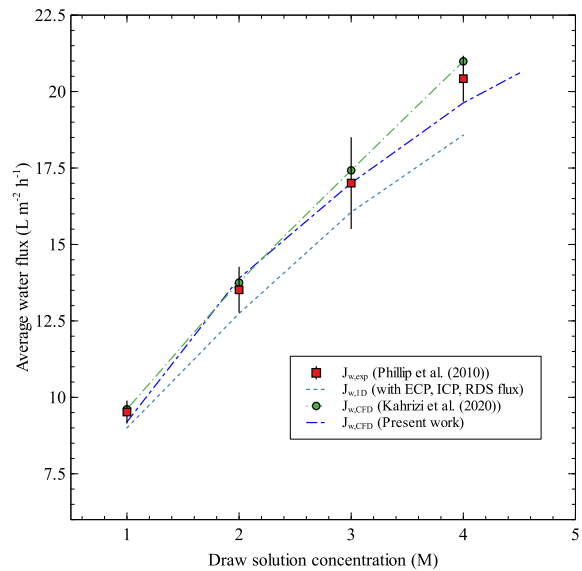


Fig. 6. Comparison of model results with other models and experimental data from Phillip et al. (2010). $c_{f,in} = 0$ (DI feed), $u_{f,in} = u_{d,in} = u^v = 0.214 m / s$, $A = 1.23 \times 10^{-12} m^2 - s / kg$, $B = 7.25 \times 10^{-8} m / s$, $\varepsilon = 0.2$, $\tau = 1.5$.

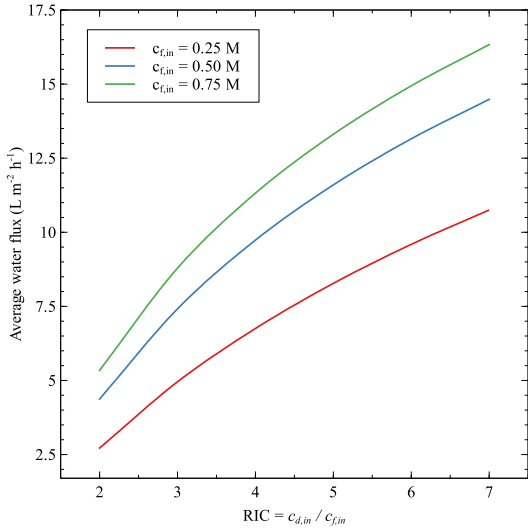


Fig. 7. Variation in $\overline{J_w}$ with the ratio of inlet concentrations (RIC) for different $c_{f,in}$. $u_{f,in} = u_{d,in} = u^V = 0.214 \text{ m/s}$, $A = 1.23 \times 10^{-12} \text{ m}^2 - \text{s/kg}$, $B = 7.25 \times 10^{-8} \text{ m/s}$, $\varepsilon = 0.2$, $\tau = 1.5$.

3.3 Variation in $\overline{J_w}$ with the ratio of inlet speeds (RIS) for co-current and counterflow conditions

Similar to section 3.2, for obtaining the effect of changing stream inlet velocities on $\overline{J_w}$, we first define the ratio of the inlet speeds (RIS) of the draw and feed streams as,

$$RIS = \frac{u_{d,in}}{u_{f,in}} \quad (15)$$

where $u_{d,in}$ and $u_{f,in}$ are the inlet speeds of the draw and the feed streams, respectively. We investigate the dependence of $\overline{J_w}$ on RIS for both co-current and countercurrent flow configurations. To ensure that the flow does not transition into turbulence in either channel, we follow the theory described in section 2.2.1 and keep the operating configuration of the module as follows:

$c_{f,in} = 0.5 \text{ M}$, $c_{d,in} = 3 \text{ M}$, $u_{f,in} = 0.02 \text{ m/s}$, $u_{d,in} = 0.02 \text{ m/s}$. The geometry of the module is kept unchanged. For both flow configurations, for $RIS > 1$, we keep $u_{f,in} = 0.02 \text{ m/s}$ and vary $u_{d,in}$ using RIS; while for $RIS < 1$, we take $u_{d,in} = 0.02 \text{ m/s}$ and vary $u_{f,in}$ through RIS.

The volumetric flow rate of a fluid stream (\dot{V}) through a channel with a cross-sectional area A can be given as,

$$\dot{V} = \iint_A \mathbf{u} \cdot \hat{n} dS \quad (16)$$

where \mathbf{u} is the fluid velocity at any point on the cross-section, \hat{n} is the unit vector on the cross-section (pointing away from the channel), and dS is a differential area element on the cross-section. If this formulation is applied to the FO module used in this study, we can notice that the flow rate depends on both the fluid velocity inside the channel and the cross-sectional area of the channel. Since both are controllable entities and can vary independently, it is not justifiable to assess the influence of changing flow rates on $\overline{J_w}$ unless the module geometry is fixed beforehand. Once the geometry is specified, the results are no longer generalizable. Hence, using inlet speeds as an independent parameter for evaluating $\overline{J_w}$ is more reasonable. The preceding discussion justifies using RIS instead of the flow rate ratio for the evaluation of FO module performance. It is crucial to note that the flow rate depends on the cross-sectional area of the duct. Given that the channel thickness is integral in determining the cross-sectional area for the flow channels in the

module used in this article, it is necessary to understand the influence of channel thicknesses on the module water flux. We perform a short investigation on the same in the appendix at the end of this article.

The results of the analysis described in the previous paragraph are presented in Fig. 8. We observe that though the countercurrent flow configuration consistently outperforms the co-current flow configuration in terms of $\overline{J_w}$, the difference is not significant, especially when $u_{f,in}$ is large when compared to $u_{d,in}$ ($RIS < 0.1$). A logarithmic scale is chosen for the x-axis to accommodate large and discrete changes in RIS. Few FO studies have focused on comprehensively assessing stream hydrodynamic effects on $\overline{J_w}$. Majeed et al. (2015) analyzed the impact of process parameters like channel flow rates on module performance. However, they assumed their feed solution to be DI water and could not capture the effects of changing flow rates on the ECP near the membrane-feed interface. On the contrary, the feed used in this study is an aqueous salt solution, and it was possible to explore the extent of the feed, membrane, and draw side concentration polarization (CP) for a better understanding of module behavior under different hydrodynamic operating conditions. Fig. 9(a) illustrates the CP observed in each flow domain of the module. For $RIS > 1$, the $\Delta\Pi$ lowering due to draw-side ECP ($\Delta\Pi_{d,ECP}$) decreases significantly with an increasing RIS, further increasing the module $\overline{J_w}$. However, the ECP decrease reduces as the flow transitions close to turbulence (based on Re_{D_h}), and a further increase in the RIS does not provide appreciable increments in $\overline{J_w}$. The incremental effect of the reduction in $\Delta\Pi_{d,ECP}$ on $\overline{J_w}$ also seems to originate at the expense of an increase in $\Delta\Pi_{ICP}$ and we can further reinforce this conclusion through Fig. 9(b). This is an essential insight into the mechanism of the rise in $\overline{J_w}$ by increasing RIS.

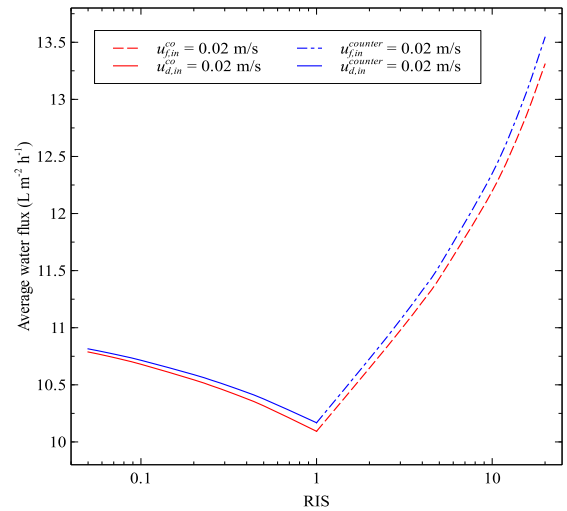


Fig. 8. Variation in $\overline{J_w}$ with RIS for co-current (red curves) and counterflow (blue curves) module configurations. $c_{f,in} = 0.5 \text{ M}$, $c_{d,in} = 3 \text{ M}$, $A = 1.23 \times 10^{-12} \text{ m}^2 - \text{s/kg}$, $B = 7.25 \times 10^{-8} \text{ m/s}$, $\varepsilon = 0.2$, $\tau = 1.5$.

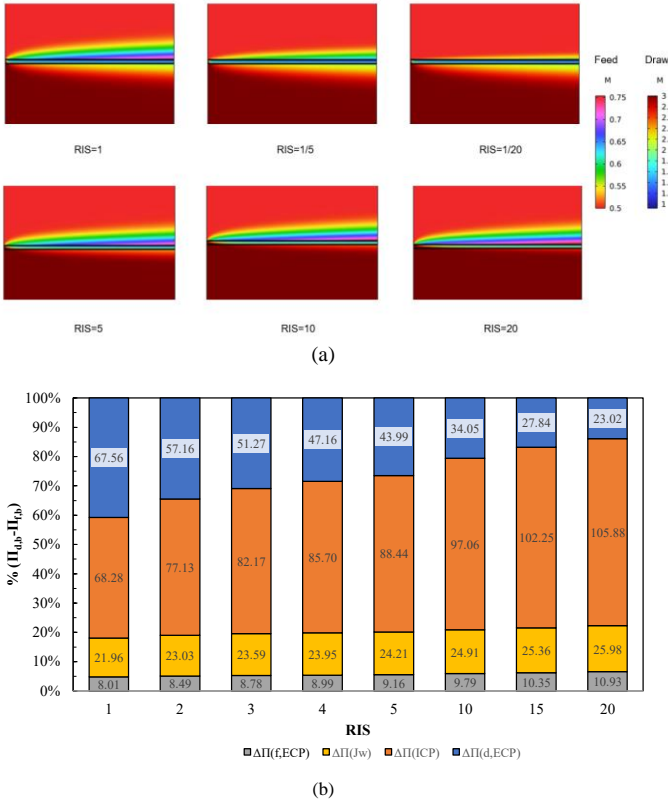


Fig. 9. (a) 2D surface plots for illustrating the aggregate CP characteristics in each domain of the module. $c_{f,in}=0.5M$, $c_{d,in}=3M$, $A=1.23\times 10^{-12}m^2-s/kg$, $B=7.25\times 10^{-8}m/s$, $\varepsilon=0.2$, $\tau=1.5$. (b) $\Delta\Pi$ observed due to the various CP phenomena in the module with a changing RIS. The y-axis represents the $\Delta\Pi$ as a percentage of $\Delta\Pi_M=\Pi_{d,b}-\Pi_{f,b}$, which is the maximum possible $\Delta\Pi$ observable in the module. The numbers within the bars indicate the value of $\Delta\Pi$ due to the relevant CP/driving force in the module (in bar). $\Delta\Pi(f,ECP)$, $\Delta\Pi(d,ECP)$, $\Delta\Pi(ICP)$, $\Delta\Pi(J_w)$ denote the osmotic pressure difference due to feed-side ECP, draw-side ECP, ICP, and the transmembrane driving force, respectively. $c_{f,in}=0.5M$, $c_{d,in}=3M$, $A=1.23\times 10^{-12}m^2-s/kg$, $B=7.25\times 10^{-8}m/s$, $\varepsilon=0.2$, $\tau=1.5$, $\Delta\Pi_M=165.81bar$, co-current flow.

To understand the longitudinal flux distribution in the base case, we demonstrate the variation in J_w along the length of the module in Fig. 10 for both co-current and counterflow configurations. The profiles have been truncated by 1 mm near the module beginning and end to accommodate for the flow development regions. In the counterflow mode, both the feed and draw concentrations increase along the membrane length (assuming $x=0$ to be the feed inlet and draw outlet) due to the continuous dewatering of the feed and dilution of the draw by the transmembrane water flux. This leads to a consistent $\Delta\Pi$ and, consequently, the flux profile when compared to the co-current module configuration, where the feed concentration keeps increasing while the draw solute concentration keeps decreasing. For relatively short modules like the base case used in our study, this difference in profiles is not significant, as the water flux decreases by 42 % from the inlet to the outlet of the feed solution for the co-current mode while it increases by 38 % for the counterflow mode. These results show that for shorter, test-scale modules like the one we use for simulations, although the average module water flux is higher in the counterflow mode than the co-current, contrary to expectations from the physics of the problem (that the local $\Delta\Pi$ is consistent for counterflow mode), there is no practical difference in the water flux vs. longitudinal position profiles for the two flow modes. We expect the observations to change significantly for longer modules because of the larger contact length between the streams.

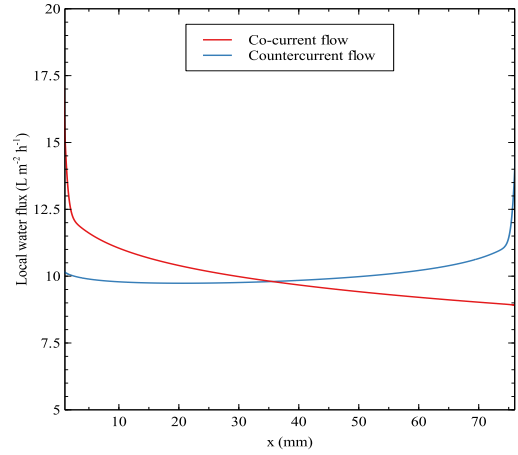


Fig. 10. Longitudinal distribution of local water flux (J_w) in the module for co-current (red) and counterflow (blue) configurations. The graph is truncated 1 mm from both ends to exclude the inlet and outlet effects on the flow regime. $c_{f,in}=0.5M$, $c_{d,in}=3M$, $u_{f,in}=u_{d,in}=0.02m/s$, $A=1.23\times 10^{-12}m^2-s/kg$, $B=7.25\times 10^{-8}m/s$, $\varepsilon=0.2$, $\tau=1.5$.

3.4 Variation in $\overline{J_w}$ with membrane parameters

From the discussion in section 2.1, it is clear that the porous support layer is much thicker than the dense selective layer and is an integral part of the FO membrane. To understand how the properties of the support layer influence the mean $\overline{J_w}$, we simulated our model for various values of support porosity (ε), tortuosity (τ), thickness (t_{PSL}), and pure water permeability (κ). It must be emphasized that all the mentioned parameters are related to the support layer, and the selective layer pure water permeability (A), as indicated in Eq. 10, is a different parameter and should not be confused with κ . Since the impact of changing ε , τ , and t_{PSL} on FO water flux has been studied up to a certain extent in previous studies [5,6], we will restrict our discussion to exploring the effects of a changing κ on mass transfer in the module. For further discussion on the effects of changing ε , τ , and t_{PSL} on FO water flux, the reader is advised to refer to the appendix at the end of this article.

Although the pure water permeability of the porous support layer (κ) is a governing parameter in Eqs. 6-7, as far as we know, there exists no systematic exploration of the effects of κ on FO module performance. In Fig. 11(a), a peculiar trend in $\overline{J_w}$ is observed with a changing support permeability (κ).

While changing κ from $10^{-15}m^2$ to $10^{-12}m^2$ barely has any noticeable effect on $\overline{J_w}$, there is a sudden increase in $\overline{J_w}$ for $\kappa > 10^{-12}m^2$. This increase in $\overline{J_w}$ is gradual for another order of magnitude (till 10^{-11}). On the contrary, $\overline{J_w}$ increases sharply for $\kappa > 10^{-11}m^2$, almost geometrically.

The increase in $\overline{J_w}$ continues for ~ 2 orders of magnitude till $\kappa \sim 10^{-9}m^2$, and then stabilizes to a constant value. Interestingly, despite κ being an intrinsic property of the membrane support, changing it does not influence the extent of ICP inside the support layer. An appreciable positive shift in the draw side ECP, however, is observed by increasing κ from $10^{-13}m^2$ to $10^{-7}m^2$ as illustrated in Fig. 11(b). Therefore, it appears that the flux enhancement observed due to an increase in κ stems from a reduction in draw-side ECP and does not support ICP. This is a surprising result, given that changing other intrinsic properties of the porous support (for example, ε , τ , t_{PSL}) necessarily influence $\overline{J_w}$ by modifying the extent of ICP in the membrane.

Based on the $\overline{J_w}$ profile in Fig. 11(a), we can define a critical support permeability, κ_c , which defines the minimum value of pure water permeability of the porous support that should be used to have the best and the most sensitive water flux performance of FO modules. We can also define an optimal support permeability, κ_o , beyond which, increasing κ has no

significant effect on the water flux. For the current module specifications, $\kappa_c = 10^{-11} m^2$, and $\kappa_o = 10^{-8} m^2$. Having κ_c and κ_o , we can also define the optimal range of κ -sensitivity (ORKS) for FO applications as $[\kappa_c, \kappa_o]$. It is crucial to understand more about the nature of the ORKS. For this purpose, we change our model configuration as flows— $u_{f,in} = u_{d,in} = \bar{u} = 0.214 m/s$ (originally, $\bar{u} = 0.02 m/s$), and $c_{f,in} = 0.5 M$, $c_{d,in} = 5 M$ (originally 3 M) and vary κ for the same range as used in Fig. 11(a). The results are described in Fig. 12(a). For $c_{d,in} = 3 M$, we observe from Fig. 11(a) that the increase in \bar{J}_w by using a membrane support layer with $\kappa = \kappa_o$ compared to a similar support layer with $\kappa < \kappa_c$ is close to 2.5 % and may be neglected for most practical purposes. However, the true advantage of using support with $\kappa = \kappa_o$ is highlighted when we change $c_{d,in}$ and \bar{u} to higher values, 5 and 0.214 m/s, respectively. Then, from Fig. 12(a), we observe a \bar{J}_w increase of more than 13.5 % when comparing the \bar{J}_w obtained for $\kappa = \kappa_o$ and $\kappa < \kappa_c$.

Another important result that can be obtained by comparing Figs. 11(a) & 12(a) is that the ORKS is apparently independent of operating conditions. This was further substantiated by simulating our model for multiple configurations with various operating conditions (not illustrated here). Again, from Fig. 12(b), we observe that a changing κ has an insignificant effect on the ICP of the membrane and the ECP on the feed side. A significant change in the ECP on the draw-side was observed for the current case. Compared to $\kappa = 2 \times 10^{-13} m^2$ (with $\Delta\Pi(d, ECP)$ being 70.27 bar), using $\kappa = 2 \times 10^{-7} m^2$ reduces the draw-side ECP significantly (the $\Delta\Pi(d, ECP)$ is 67.56 bar). Through the preceding discussion, we can conclusively say that the ORKS is a critical, configuration-invariant performance control parameter for FO module performance. An accurate determination of ORKS will also prevent overdesign situations where κ is made unnecessarily high to enhance \bar{J}_w even though the gain in \bar{J}_w obtained by increasing κ stops as κ reaches κ_o .

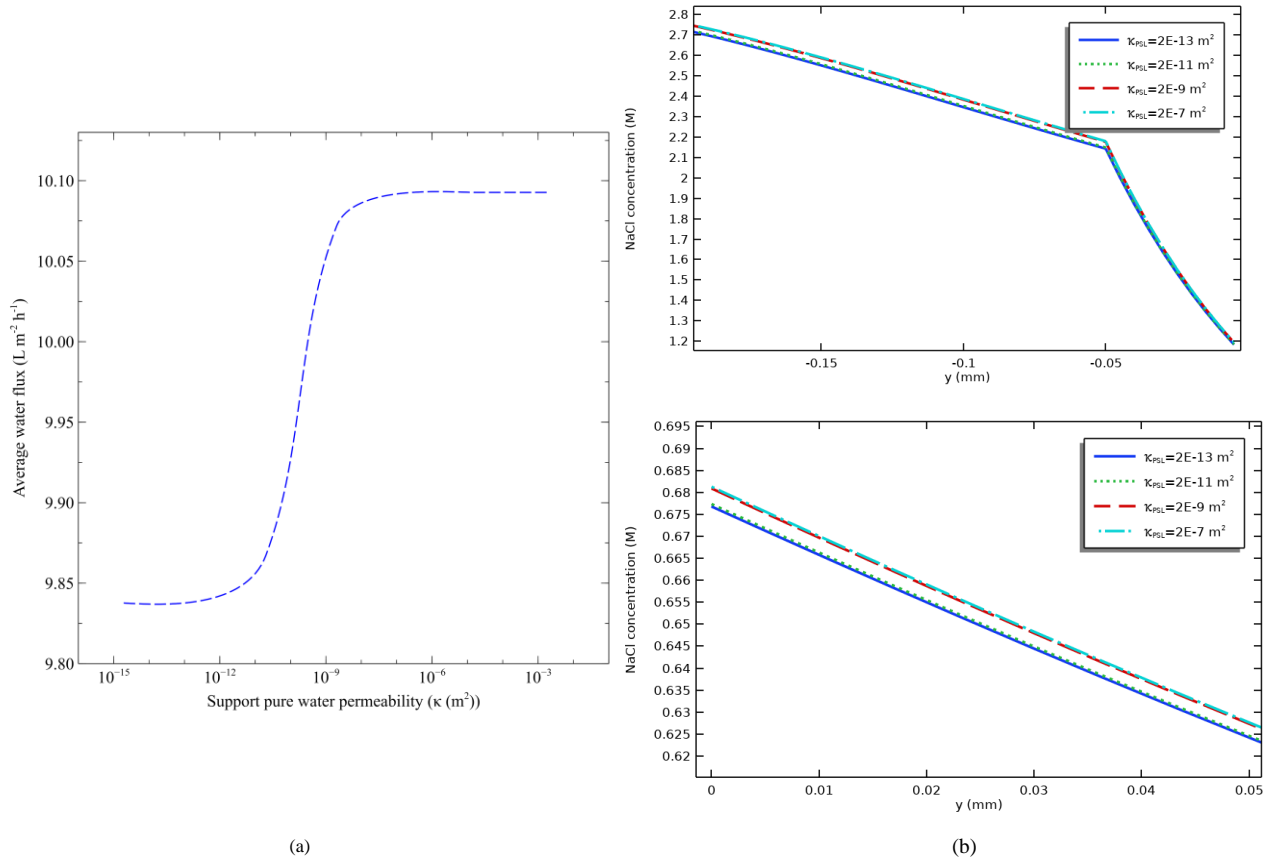


Fig. 11. Variation in \bar{J}_w with membrane support layer property κ and the corresponding CP plots for the base configuration. (a) κ (b) Module CP with varying κ . $c_{f,in} = 0.5 M$, $c_{d,in} = 3 M$, $u_{f,in} = u_{d,in} = 0.02 m/s$, (co-current flow), $A = 1.23 \times 10^{-12} m^2.s/kg$, $B = 7.25 \times 10^{-8} m/s$.

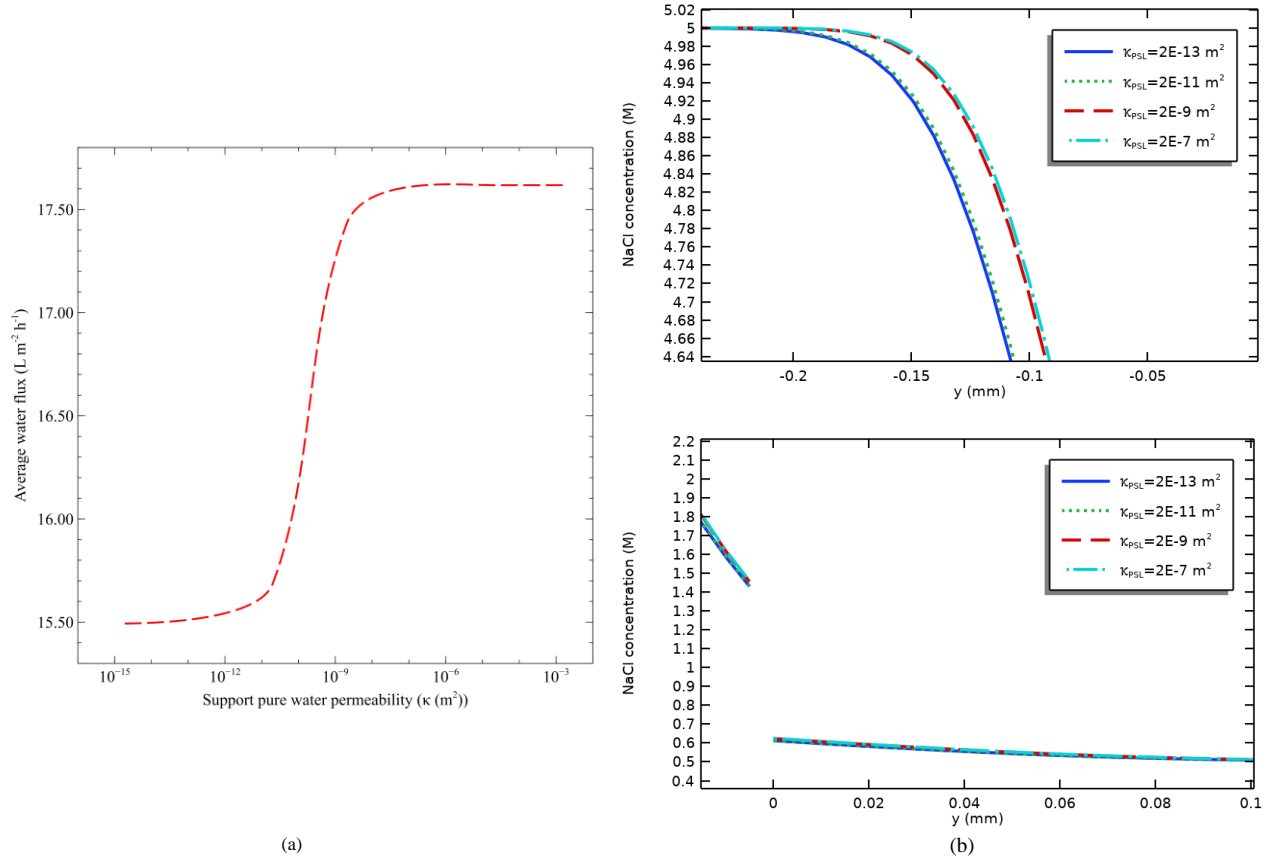


Fig. 12. (a) Variation in $\overline{J_w}$ with κ ; and (b) the corresponding module CP plots for the base configuration with $c_{d,in}$ increased to $5M$. $c_{f,in}=0.5M$, $c_{d,in}=5M$, $u_{f,in}=u_{d,in}=0.02 \text{ m/s}$ (co-current flow), $A=1.23 \times 10^{-12} \text{ m}^2 \cdot \text{s/kg}$, $B=7.25 \times 10^{-8} \text{ m/s}$.

3.5 Investigations on the membrane modeling index, S^*

Substituting the values of the constituent membrane support parameters used in the base case into the expressions for S and S^* , we find that $S = 375 \mu\text{m}$, and $S^* = 667 \mu\text{m}$. Since both values are comparable, none can be neglected while modeling the FO system. However, if κ is three orders smaller, then $S^* = 0.667 \mu\text{m}$, $S^* \ll S$, and the viscous terms in Eq. 13 may be conveniently neglected. This would reduce Eq. 13 to a Darcy-type formulation and reduce computational costs.

The discussion can be leveraged to justify the existence of the ORKS. On the one hand, for $\kappa < \kappa_c$, $S^* \ll S$, and the Darcian nature of the flow inside the porous support dominates the viscosity-driven flow, and the water flux experiences no change with the changing value of κ . On the other hand, for $\kappa \geq \kappa_c$, $S^* \gg S$, and the flow inside the membrane is dominated by the viscous effects exerted by the bulk flowing draw solution. Again, the water flux does not increase by a further increase in κ . This implies that only when the Darcian terms have a magnitude comparable to the viscous terms (both within three orders of magnitude of each other) can a change in κ have a significant impact on J_w , and the magnitudes can be ascertained by evaluating S^* .

While S^* is helpful for CFD modeling, unlike S , it does not seem to have much relevance while determining $\overline{J_w}$. The influence of S on $\overline{J_w}$ in FO systems has been discussed thoroughly elsewhere [28,34–37]. In Fig. 13, we illustrate the variation in $\overline{J_w}$ with a changing S^* . Clearly, there exists no predictable trend in $\overline{J_w}$ with an increasing S^* . Instead, it is much more insightful to understand the effects of changing individual support layer properties as we do in section 3.4 and the appendix.

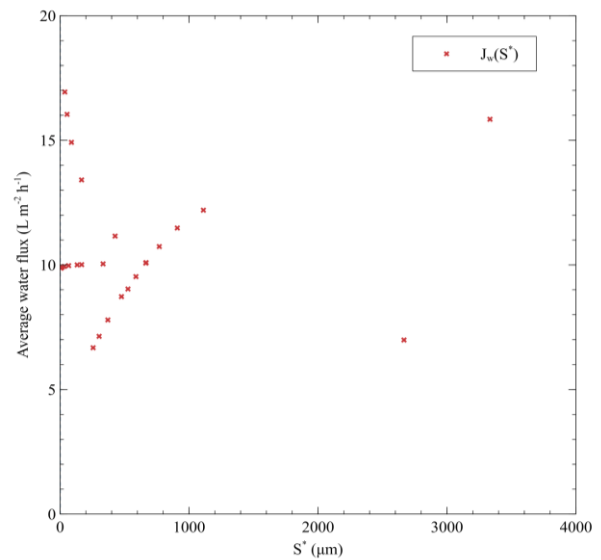


Fig. 13. Exploring the relevance of the membrane modeling index, S^* , to module performance by graphing the variation in $\overline{J_w}$ with a varying S^* . S^* was changed by changing each of its constituent parameters randomly. $S^* > 0 \forall \varepsilon, \tau, t_{PSL}, \kappa$. $c_{f,in}=0.5M$, $c_{d,in}=3M$, $u_{f,in}=u_{d,in}=0.02 \text{ m/s}$ (co-current flow), $A=1.23 \times 10^{-12} \text{ m}^2 \cdot \text{s/kg}$, $B=7.25 \times 10^{-8} \text{ m/s}$.

4. Conclusions

We developed a 2D, grid-independent finite element model for evaluating the performance of FO modules for diverse ranges of system parameters. The key insights from our study are summarized as follows-

1. Previous publications have explored the effects of $c_{f,in}$ and $c_{d,in}$ on FO performance independent of each other [5,6,8,12]. We suggest a single parameter, the RIC, to quantify the relative imbalance in magnitudes of $c_{f,in}$ and $c_{d,in}$. We find that significant benefits in the average module water flux can be obtained by increasing the RIC when $c_{f,in}$ is relatively low.

2. Since the flow rate is formulated using both inlet speed and cross-sectional area, we recommend using the RIS instead of the conventional flow rate ratio to evaluate FO performance. Although the counterflow operation mode consistently outperforms the co-current mode for all RIS, the difference is insignificant for low RIS (<0.1). For $RIS > 1$, $\overline{J_w}$ increases with an increasing RIS. The mechanism of this increase was found to be the reduction of draw-side ECP at the expense of an increasing membrane ICP. We also find that the longitudinal J_w profile is flatter for the counterflow module configuration compared to its co-current counterpart. However, this dissimilarity is only significant for long modules and is not conspicuous in the present study.

3. We understand module behavior as a function of membrane support properties. The novelty here is that we investigate the effects of κ on module performance, a task that has not been undertaken previously. We suggest the existence of an ORKS, a configuration-invariant parameter control range, outside which the FO module is insensitive to changes in κ . For the current study, the ORKS is $[10^{-11} m^2, 10^{-8} m^2]$. Accurately determining the ORKS via CFD can help find the optimal value of κ and prevent overdesign situations where κ is unnecessarily increased beyond the ORKS in a futile bid to increase the water flux.

4. Our study concludes by proposing a membrane modeling index, S^* , that can be compared with the membrane structural parameter, S , to identify what type of governing equations should be used for modeling fluid flow inside the porous support and if there is any possibility of reducing the solution time by a judicious choice of the fluid flow model. For our base case, $S = 375 \mu m$ and $S^* = 667 \mu m$. Since both parameters are comparable in magnitude, we have no choice but to use the computationally expensive Brinkman formulation for support modeling. However, if S^* were to be $0.667 \mu m$ (three orders smaller), we could have switched to a Darcy-type model and saved valuable computation time. S^* is expected to have a higher significance for support modeling when the number of grid elements is much larger than ours. We also observe a noteworthy limitation in the application of S^* . Based on the present work, we do not see any role of S^* in determining $\overline{J_w}$. As of now, it seems to be a pure modeling construct. Future studies may explore the existence of a unified membrane parameter, say X , that combines ε , τ , t_{PSL} , and κ into a single formula.

Nomenclature

A	Pure water permeability of the selective layer
B	Draw solute permeability of the selective layer
c	Solute concentration
D	Diffusion coefficient
J	Flux
k	Mass transfer coefficient
L	Module length
Re	Reynolds' number
S	Membrane structural parameter
S^*	Membrane modeling index
t	Thickness
u	Longitudinal velocity magnitude
v	Transverse velocity magnitude

Greek symbols

ε	Porosity of the support layer
κ	Pure water permeability of the support layer
μ	Dynamic viscosity
ρ	Density
τ	Tortuosity of the support layer
Π	Osmotic pressure
Subscripts	
in	Inlet
f	Feed
d	Draw
PSL	Porous support layer
c	Solute concentration
m	Membrane
b	Bulk
i	Interface of the selective and support layers

Acknowledgment

The author Shivang Rampriyan would like to thank the PMRF funding from Ministry of Education, Government of India for performing this study.

Credit authorship contribution statement

S. Rampriyan: Conceptualization; Data curation; Formal analysis; Investigation; Methodology; Resources; Software; Validation; Visualization; Writing – original draft; Writing – review & editing.
B. Ray: Investigation; Methodology; Supervision; Writing – review & editing; Resources.

Funding sources

This research did not receive any specific grant from funding agencies in the public, commercial, or not-for-profit sectors.

Declaration of Competing Interest

The authors declare that they have no known competing financial interests or personal relationships that could have appeared to influence the work reported in this paper.

References

- [1] T.S. Chung, L. Luo, C.F. Wan, Y. Cui, G. Amy, What is next for forward osmosis (FO) and pressure retarded osmosis (PRO), Sep. Purif. Technol. 156 (2015) 856–860. <https://doi.org/10.1016/j.seppur.2015.10.063>.
- [2] Q. She, R. Wang, A.G. Fane, C.Y. Tang, Membrane fouling in osmotically driven membrane processes: A review, J. Memb. Sci. 499 (2016) 201–233. <https://doi.org/10.1016/j.memsci.2015.10.040>.
- [3] B. Mi, M. Elimelech, Organic fouling of forward osmosis membranes: Fouling reversibility and cleaning without chemical reagents, J. Memb. Sci. 348 (2010) 337–345. <https://doi.org/10.1016/j.memsci.2009.11.021>.
- [4] M. Mohammadifakhr, J. de Grooth, H.D.W. Roesink, A.J.B. Kemperman, Forward osmosis: A critical review, Processes. 8 (2020) 404. <https://doi.org/10.3390/PR8040404>.
- [5] M. Kahrizi, J. Lin, G. Ji, L. Kong, C. Song, L.F. Dumée, S. Sahebi, S. Zhao, Relating forward water and reverse salt fluxes to membrane porosity and tortuosity in forward osmosis: CFD modelling, Sep. Purif. Technol. 241 (2020) 116727. <https://doi.org/10.1016/j.seppur.2020.116727>.
- [6] J. Ren, M.R. Chowdhury, L. Xia, C. Ma, G.M. Bollas, J.R. McCutcheon, A computational fluid dynamics model to predict performance of hollow fiber membrane modules in forward osmosis, J. Memb. Sci. 603 (2020) 117973.

- [7] <https://doi.org/10.1016/j.memsci.2020.117973>.
M.F. Gruber, C.J. Johnson, C.Y. Tang, M.H. Jensen, L. Yde, C. Hélix-Nielsen, Computational fluid dynamics simulations of flow and concentration polarization in forward osmosis membrane systems, *J. Memb. Sci.* 379 (2011) 488–495. <https://doi.org/10.1016/j.memsci.2011.06.022>.
- [8] A. Sagiv, A. Zhu, P.D. Christofides, Y. Cohen, R. Semiat, Analysis of forward osmosis desalination via two-dimensional FEM model, *J. Memb. Sci.* 464 (2014) 161–172. <https://doi.org/10.1016/j.memsci.2014.04.001>.
- [9] J.O. Kessler, C.D. Moody, Drinking water from sea water by forward osmosis, *Desalination*. 18 (1976) 297–306. [https://doi.org/10.1016/S0011-9164\(00\)84119-3](https://doi.org/10.1016/S0011-9164(00)84119-3).
- [10] C. Suh, S. Lee, Modeling reverse draw solute flux in forward osmosis with external concentration polarization in both sides of the draw and feed solution, *J. Memb. Sci.* 427 (2013) 365–374. <https://doi.org/10.1016/j.memsci.2012.08.033>.
- [11] J.R. McCutcheon, M. Elimelech, Modeling water flux in forward osmosis: Implications for improved membrane design, *AIChE J.* 53 (2007) 1736–1744. <https://doi.org/10.1002/aic.11197>.
- [12] W.A. Phillip, J.S. Yong, M. Elimelech, Reverse draw solute permeation in forward osmosis: Modeling and experiments, *Environ. Sci. Technol.* 44 (2010) 5170–5176. <https://doi.org/10.1021/es100901n>.
- [13] D. Attarde, M. Jain, S.K. Gupta, Modeling of a forward osmosis and a pressure-retarded osmosis spiral wound module using the Spiegler-Kedem model and experimental validation, *Sep. Purif. Technol.* 164 (2016) 182–197. <https://doi.org/10.1016/j.seppur.2016.03.039>.
- [14] M. Sekino, Mass transport analysis of a hollow fiber forward osmosis module via two-layer membrane model derived from the irreversible thermodynamics, *Chem. Eng. Sci.* 247 (2022) 116703. <https://doi.org/10.1016/J.CES.2021.116703>.
- [15] M. Kahrizi, N. Kasiri, T. Mohammadi, S. Zhao, Introducing sorption coefficient through extended UNIQUAC and Flory-Huggins models for improved flux prediction in forward osmosis, *Chem. Eng. Sci.* 198 (2019) 33–42. <https://doi.org/10.1016/J.CES.2018.11.056>.
- [16] Y.Y. Liang, D.F. Fletcher, Computational fluid dynamics simulation of forward osmosis (FO) membrane systems: Methodology, state of art, challenges and opportunities, *Desalination*. 549 (2023) 116359. <https://doi.org/10.1016/j.desal.2022.116359>.
- [17] K.Y. Toh, Y.Y. Liang, W.J. Lau, G.A. Fimbres Weihs, A review of CFD modelling and performance metrics for osmotic membrane processes, *Membranes (Basel)*. 10 (2020) 1–30. <https://doi.org/10.3390/membranes10100285>.
- [18] M. Bahoosh, E. Kashi, S. Shokrollahzadeh, The side stream and different spacers effects on the permeate water flux in forward osmosis process using computational fluid dynamics, *Chem. Eng. Process. - Process Intensif.* 181 (2022) 109113. <https://doi.org/10.1016/j.cep.2022.109113>.
- [19] J. Benjamin, S. AL Mashrafi, A. Tejada-Martinez, N. Diaz-Elsayed, M.E. Arias, Q. Zhang, Optimizing pressure retarded osmosis spacer geometries: An experimental and CFD modeling study, *J. Memb. Sci.* 647 (2022) 120284. <https://doi.org/10.1016/j.memsci.2022.120284>.
- [20] V. Pozzobon, P. Perré, Mass transfer in hollow fiber membrane contactor: Computational fluid dynamics determination of the shell side resistance, *Sep. Purif. Technol.* 241 (2020) 116674. <https://doi.org/10.1016/j.seppur.2020.116674>.
- [21] Z.M. Binger, A. Achilli, Surrogate modeling of pressure loss & mass transfer in membrane channels via coupling of computational fluid dynamics and machine learning, *Desalination*. 548 (2023) 116241. <https://doi.org/10.1016/j.desal.2022.116241>.
- [22] S. Bae, B. Gu, J.H. Lee, A 3D CFD study on the effects of feed spacer designs on membrane performance for high-permeance RO membranes, *J. Water Process Eng.* 53 (2023) 103887. <https://doi.org/10.1016/j.jwpe.2023.103887>.
- [23] Q. Yang, Y. Heng, Y. Jiang, J. Luo, Multiscale Analysis of Permeable and Impermeable Wall Models for Seawater Reverse Osmosis Desalination, *Separations*. 10 (2023) 134. <https://doi.org/10.3390/separations10020134>.
- [24] Y.K. Chong, Y.Y. Liang, G.A.F. Weihs, Validation and characterisation of mass transfer of 3D-CFD model for twisted feed spacer, *Desalination*. 554 (2023) 116516. <https://doi.org/10.1016/j.desal.2023.116516>.
- [25] E.W. Tow, R.K. McGovern, J.H. Lienhard V, Raising forward osmosis brine concentration efficiency through flow rate optimization, *Desalination*. 366 (2015) 71–79. <https://doi.org/10.1016/j.desal.2014.10.034>.
- [26] N.Y. Yip, M. Elimelech, Performance Limiting Effects in Power Generation from Salinity Gradients by Pressure Retarded Osmosis, *Environ. Sci. Technol.* 45 (2011) 10273–10282. <https://doi.org/10.1021/es203197e>.
- [27] N.Y. Yip, A. Tiraferri, W.A. Phillip, J.D. Schiffman, M. Elimelech, High performance thin-film composite forward osmosis membrane, *Environ. Sci. Technol.* 44 (2010) 3812–3818. <https://doi.org/10.1021/es1002555>.
- [28] N.N. Bui, J.T. Arena, J.R. McCutcheon, Proper accounting of mass transfer resistances in forward osmosis: Improving the accuracy of model predictions of structural parameter, *J. Memb. Sci.* 492 (2015) 289–302. <https://doi.org/10.1016/j.memsci.2015.02.001>.
- [29] S. Xia, L. Yao, R. Yang, Y. Zhou, Organic fouling in forward osmosis (FO): Membrane flux behavior and foulant quantification, *Membr. Water Treat.* 6 (2015) 161–172. <https://doi.org/10.12989/mwt.2015.6.2.161>.
- [30] E. V. Mosina, Numerical study of flow at a liquid-porous medium interface, *Theor. Found. Chem. Eng.* 2010 445. 44 (2010) 679–685. <https://doi.org/10.1134/S0040579510050076>.
- [31] S. Phunsho, H.K. Shon, S. Hong, S. Lee, S. Vigneswaran, A novel low energy fertilizer driven forward osmosis desalination for direct fertigation: Evaluating the performance of fertilizer draw solutions, *J. Memb. Sci.* 375 (2011) 172–181. <https://doi.org/10.1016/j.memsci.2011.03.038>.
- [32] D.L. Shaffer, J.R. Werber, H. Jaramillo, S. Lin, M. Elimelech, Forward osmosis: Where are we now?, *Desalination*. 356 (2015) 271–284. <https://doi.org/10.1016/j.desal.2014.10.031>.
- [33] M.A. Darwish, H.K. Abdulrahim, A.S. Hassan, A.A. Mabrouk, A.O. Sharif, The forward osmosis and desalination, *Desalin. Water Treat.* 57 (2016) 4269–4295. <https://doi.org/10.1080/19443994.2014.995140>.
- [34] A. Tiraferri, N.Y. Yip, A.P. Straub, S. Romero-Vargas Castrillon, M. Elimelech, A method for the simultaneous determination of transport and structural parameters of forward osmosis membranes, *J. Memb. Sci.* 444 (2013) 523–538. <https://doi.org/10.1016/j.memsci.2013.05.023>.
- [35] B. Kim, G. Gwak, S. Hong, Review on methodology for determining forward osmosis (FO) membrane characteristics: Water permeability (A), solute permeability (B), and structural parameter (S), *Desalination*. 422 (2017) 5–16. <https://doi.org/10.1016/j.desal.2017.08.006>.
- [36] M. Park, J.J. Lee, S. Lee, J.H. Kim, Determination of a constant membrane structure parameter in forward osmosis processes, *J. Memb. Sci.* 375 (2011) 241–248. <https://doi.org/10.1016/j.memsci.2011.03.052>.
- [37] S. Loeb, L. Titelman, E. Korngold, J. Freiman, Effect of porous support fabric on osmosis through a Loeb-Sourirajan type asymmetric membrane, *J. Memb. Sci.* 129 (1997) 243–249. [https://doi.org/10.1016/S0376-7388\(96\)00354-7](https://doi.org/10.1016/S0376-7388(96)00354-7).

Appendix

A. Variation in \bar{J}_w with the thicknesses of the feed and draw channels

While several FO studies have focused on understanding the variation in \bar{J}_w with the flow rates of the feed and draw streams (Hawari et al., 2016; Im et al., 2018; Lee et al., 2010; Majeed et al., 2015; Tan & Ng, 2008; Xu et al., 2010), as far as we are aware, none of them have analyzed the effects of changing channel thicknesses on the module water flux. From Eq. 16, the flow rates of the channels depend on both the inlet velocity and the thickness of the channel. While the former was dealt with in section 3.3, the current section is focused on the effects of changing channel thicknesses on the transmembrane water flux, \bar{J}_w .

Unlike previous cases, where we combined the feed and draw side parameters into a ratio, here we vary the thicknesses of the feed ($t_{c,f}$) and draw ($t_{c,d}$) channels independent of each other. Both $t_{c,f}$ and $t_{c,d}$ were varied from 1.5 mm to 6 mm in steps of 0.75 mm, and the respective values of \bar{J}_w were recorded to generate Fig. A1. The inlet flow speeds of both the feed and draw channels were fixed at $\bar{u} = 0.02 \text{ m/s}$ and the module was operated in counterflow mode. Fig. A1 illustrates a general decreasing trend in \bar{J}_w with increasing channel thickness, regardless of the channel considered. This can be explained as follows. In a closed channel flow, as in our module, the maximum thickness of a velocity boundary layer (magnitude scale) can be $\delta_{max} = t_{c,i}/2$, where i can be f or d for the feed and the draw channels, respectively. This means that for thin channels, the velocity boundary layer at the membrane surface can grow less compared to thick channels. Since the velocity and concentration profiles are closely related (see Eq. 8), it is safe to remark that when $t_{c,i}$ takes a lower value, the concentration boundary layer is thin when compared to thick channels with high $t_{c,i}$. This implies a lower level of CP in the module and a lesser reduction in the effective driving force. Overall, we expect the water flux to increase for thinner channels, which is well demonstrated in Fig. A1.

From Fig. A1, it is also clear that \bar{J}_w is more sensitive to changes in $t_{c,d}$ than $t_{c,f}$. For example, for $t_{c,f} = 1.5 \text{ mm}$, as we increase $t_{c,d}$ from 1.5 mm to 6 mm, \bar{J}_w decreases by nearly 9 % from 10.86 LMH to 9.87 LMH. Instead, if we keep $t_{c,d} = 1.5 \text{ mm}$ and vary $t_{c,f}$ from 1.5 mm to 6 mm, it can be seen that \bar{J}_w decreases by only ~4 %, from 10.86 LMH to 10.41 LMH. Therefore, if the intention is to control the module output flux by changing the channel thickness, one must emphasize more on the control of the draw channel thickness rather than the feed channel thickness. This can be explained by observing the CP in the module. Based on the preceding discussion, the draw channel thickness controls both the ICP in the porous support and the ECP on the membrane-draw solution interface. So, reducing $t_{c,d}$ will reduce both membrane ICP and draw-side ECP. However, reducing the feed channel thickness affects only the ECP on the feed side, which is marginal and often neglected in FO models due to low \bar{J}_w values (Gu et al., 2011; Tan & Ng, 2008). Since the draw channel thickness affects both ICP and ECP, it exerts a greater influence over \bar{J}_w . The CP observed in the module is further exemplified through Figs. A2(a) and (b), which provide additional credibility to our arguments. It is evident from Fig. A2(b) that at a constant $t_{c,d}$, a reducing $t_{c,f}$ has negligible effects on improving the transmembrane driving force when compared to fixing $t_{c,f}$ and reducing $t_{c,d}$ (see Fig. A2(a)).

It is interesting to note that reducing $t_{c,i}$ at a constant channel inlet speed ultimately reduces the operating flow rate. The flow rate may also be reduced by decreasing the inlet speed while keeping the channel thickness constant. The water flux, \bar{J}_w , increases in the former case while decreases in the latter, even though the flow rate decreases in both cases. Unless the flow rate is resolved into inlet speed and channel thickness and their effects on \bar{J}_w are analyzed separately, one might be tempted to incorrectly conclude that reducing the flow rate reduces the average water flux in the module, as seen in Gu et al. (2011). So, if the intent is to control module performance through channel thicknesses, we must prioritize $t_{c,d}$. Arriving at this insight experimentally is tedious, requiring the production of multiple modules of different dimensions. In this study, we eliminate the design and manufacturing costs and elucidate the true advantage of using CFD to evaluate FO systems.

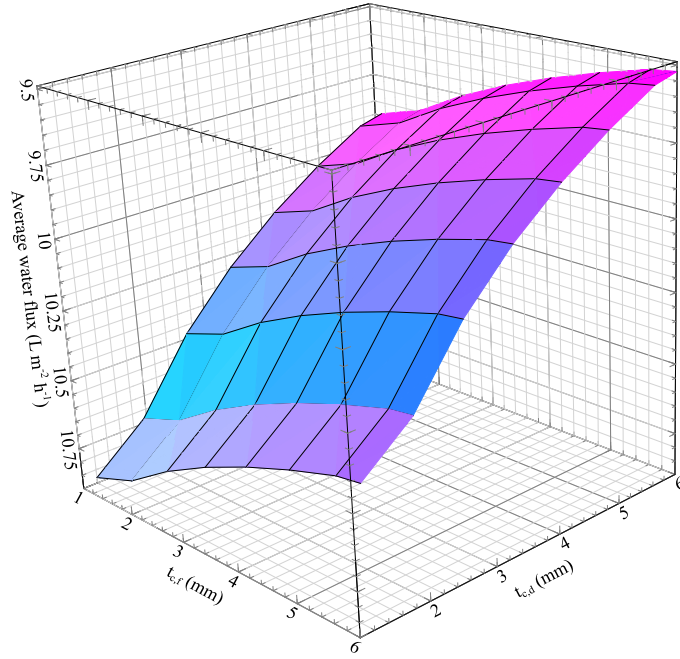


Fig. A1. Variation in \bar{J}_w with the feed and draw channel thicknesses. The module was operated in counterflow mode. $c_{f,in} = 0.5 M$, $c_{d,in} = 3 M$, $u_{f,in} = u_{d,in} = 0.02 m/s$, $A = 1.23 \times 10^{-12} m^2 - s/kg$, $B = 7.25 \times 10^{-8} m/s$, $\varepsilon = 0.2$, $\tau = 1.5$.

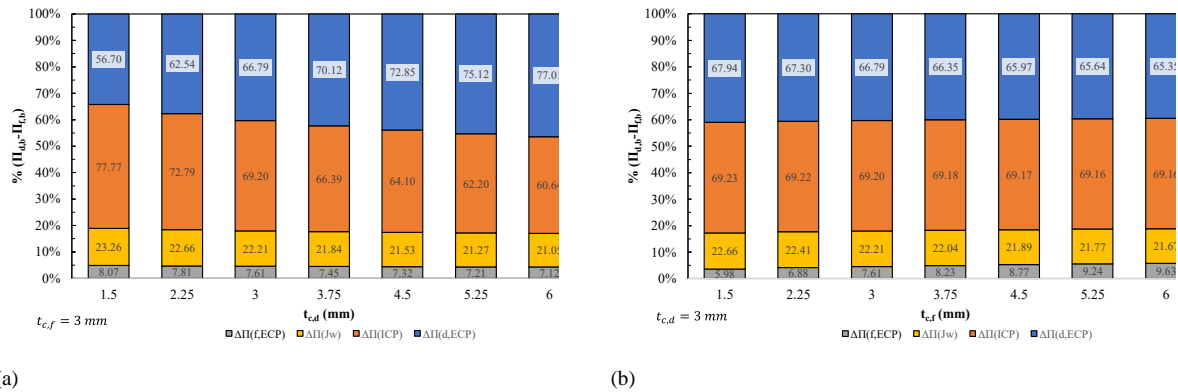
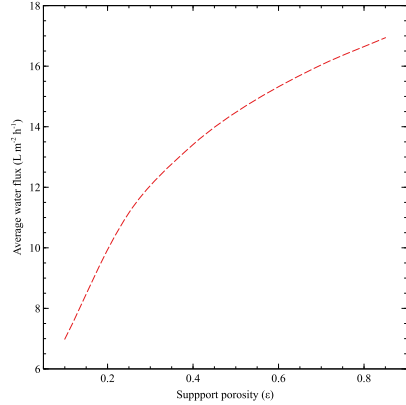


Fig. A2. $\Delta\Pi$ observed due to the various CP phenomena existing in the module with a changing $t_{c,i}$ ($i = f, d$). The y-axis represents the $\Delta\Pi$ as a percentage of $\Delta\Pi_M = \Pi_{d,b} - \Pi_{f,b}$, which is the maximum possible $\Delta\Pi$ observable in the module. The numbers within the bars indicate the value of $\Delta\Pi$ due to the relevant CP/driving force in the module (in bar). $\Delta\Pi(f, ECP)$, $\Delta\Pi(d, ECP)$, $\Delta\Pi(ICP)$, $\Delta\Pi(J_w)$ denote the osmotic pressure difference due to feed-side ECP, draw-side ECP, ICP, and the transmembrane driving force, respectively. (a) Corresponding $\Delta\Pi$ in the module with a varying $t_{c,d}$ at $t_{c,f} = 3 mm$; (b) Corresponding $\Delta\Pi$ in the module with a varying $t_{c,f}$ at $t_{c,d} = 3 mm$. $c_{f,in} = 0.5 M$, $c_{d,in} = 3 M$, $u_{f,in} = u_{d,in} = 0.02 m/s$ (counterflow), $A = 1.23 \times 10^{-12} m^2 - s/kg$, $B = 7.25 \times 10^{-8} m/s$, $\varepsilon = 0.2$, $\tau = 1.5$, $\Delta\Pi_M = 165.81 bar$.

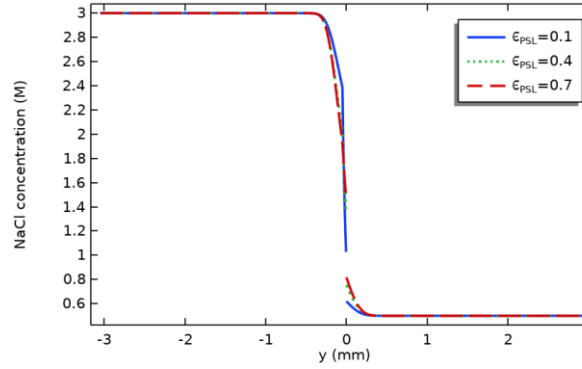
B. Variation in \bar{J}_w with common membrane parameters

From Fig. B1(a), we can observe that \bar{J}_w increases with ε . At lower values of ε , this increase is sharper than that at its higher values. In our simulations, ε was varied from 0.1 to 0.85, and it was observed that the corresponding \bar{J}_w increases by more than 140 %, from 6.99 LMH to 16.94 LMH. To understand the reasoning behind this observation, we plot the solute concentration profile obtained at the middle of the module ($x = L/2$) in Fig. B1(b). Due to an increase in the concentrative ECP on the feed side with an increasing ε , \bar{J}_w increases. A similar trend is observed on the draw side, where the dilutive ECP increases, leading to a further lower osmotic pressure at the feed-membrane interface. While ECP increases on both sides of the membrane at higher porosity, the support layer ICP decreases, which ensures a higher \bar{J}_w . An increased porosity implies an increased void volume and an equivalently higher draw solution permeation (given other membrane properties are constant), leading to a reduced solute resistivity and CP. Similar findings have been reported by Kahrizi et al. (2020). Another interesting insight from Fig. B(a) is that \bar{J}_w is highly sensitive to ε at lower values of ε than at its higher values. For example, increasing ε from 0.1 to 0.4 increases \bar{J}_w by ~92% from 6.99 LMH to 13.41 LMH, while increasing ε by the same amount from 0.55 to 0.85 produces a mere ~14 % increase in \bar{J}_w . Therefore, while huge gains in \bar{J}_w can be obtained by perturbing ε around its lower values, there is not much utility in increasing an already high support porosity. From these observations, we can conclude that ICP generally outweighs ECP in determining module water flux performance and that the intrinsic properties of the support layer significantly influence

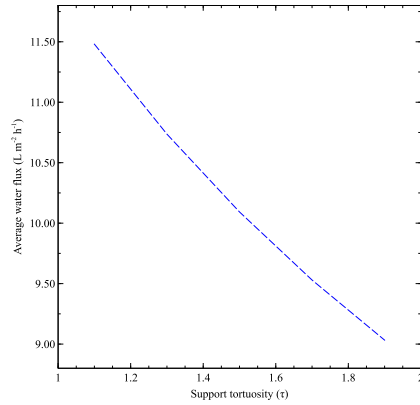
the ICP. This argument is further substantiated in Figs. B1(c)-(d) and B1(e)-(f), which illustrate that \bar{J}_w decreases with increasing support tortuosity or thickness. Both τ and t_{PSL} are directly associated with the membrane support's resistivity to solute diffusion and, consequently, the ICP observed (McCutcheon & Elimelech, 2006), which explains the observations (see Figs. B1(d), (f) for visualizing the module CP). While the flux varies almost linearly with τ , so is not the case with t_{PSL} . At lower values of t_{PSL} , \bar{J}_w is highly sensitive to t_{PSL} . Contrastingly, the gain in \bar{J}_w by reducing t_{PSL} is not significant at its higher values. Thin supports reduce the ICP while keeping ample scope for enhancing the average water flux by small negative perturbations in t_{PSL} . Similar recommendations are made in other studies (McCutcheon & Elimelech, 2007; Tiraferri et al., 2011; Yip et al., 2010).



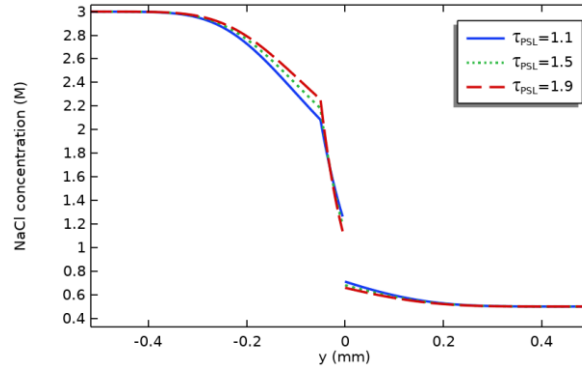
(a)



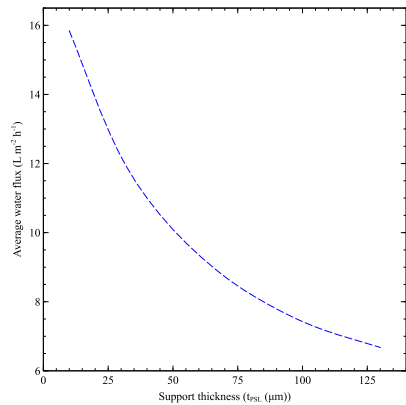
(b)



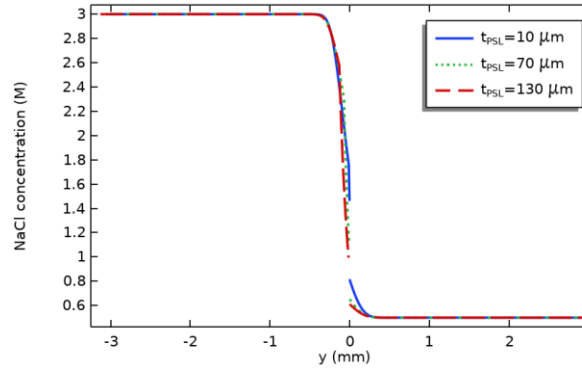
(c)



(d)



(e)



(f)

Fig. B1. Variation in \bar{J}_w with membrane support layer properties like ϵ , τ , t_{PSL} , and the corresponding CP plots for the base configuration. (a) ϵ (b) Module CP with varying ϵ (c) τ (d) Module CP with varying τ (e) t_{PSL} (f) Module CP with varying t_{PSL} . $c_{f,in} = 0.5 M$, $c_{d,in} = 3 M$, $u_{f,in} = u_{d,in} = 0.02 m/s$, (co-current flow), $A = 1.23 \times 10^{-12} m^2 - s/kg$, $B = 7.25 \times 10^{-8} m/s$.

References

- Gu, B., Kim, D. Y., Kim, J. H., & Yang, D. R. (2011). Mathematical model of flat sheet membrane modules for FO process: Plate-and-frame module and spiral-wound module. *Journal of Membrane Science*, 379(1–2), 403–415. <https://doi.org/10.1016/j.memsci.2011.06.012>
- Hawari, A. H., Kamal, N., & Altaee, A. (2016). Combined influence of temperature and flow rate of feeds on the performance of forward osmosis. *Desalination*, 398, 98–105. <https://doi.org/10.1016/j.desal.2016.07.023>
- Im, S. J., Jeong, S., & Jang, A. (2018). Feasibility evaluation of element scale forward osmosis for direct connection with reverse osmosis. *Journal of Membrane Science*, 549, 366–376. <https://doi.org/10.1016/j.memsci.2017.12.027>
- Lee, S., Boo, C., Elimelech, M., & Hong, S. (2010). Comparison of fouling behavior in forward osmosis (FO) and reverse osmosis (RO). *Journal of Membrane Science*, 365(1–2), 34–39. <https://doi.org/10.1016/j.memsci.2010.08.036>
- Majeed, T., Phuntsho, S., Sahebi, S., Kim, J. E., Yoon, J. K., Kim, K., & Shon, H. K. (2015). Influence of the process parameters on hollow fiber-forward osmosis membrane performances. *Desalination and Water Treatment*, 54(4–5), 817–828. <https://doi.org/10.1080/19443994.2014.916232>
- McCutcheon, J. R., & Elimelech, M. (2007). Modeling water flux in forward osmosis: Implications for improved membrane design. *AIChE Journal*, 53(7), 1736–1744. <https://doi.org/10.1002/aic.11197>
- McCutcheon, J. R., & Elimelech, M. (2006). Influence of concentrative and dilutive internal concentration polarization on flux behavior in forward osmosis. *Journal of Membrane Science*, 284(1–2), 237–247. <https://doi.org/10.1016/j.memsci.2006.07.049>
- Tan, C. H., & Ng, H. Y. (2008). Modified models to predict flux behavior in forward osmosis in consideration of external and internal concentration polarizations. *Journal of Membrane Science*, 324(1–2), 209–219. <https://doi.org/10.1016/j.memsci.2008.07.020>
- Tiraferri, A., Yip, N. Y., Phillip, W. A., Schiffman, J. D., & Elimelech, M. (2011). Relating performance of thin-film composite forward osmosis membranes to support layer formation and structure. *Journal of Membrane Science*, 367(1–2), 340–352. <https://doi.org/10.1016/J.MEMSCI.2010.11.014>
- Xu, Y., Peng, X., Tang, C. Y., Fu, Q. S., & Nie, S. (2010). Effect of draw solution concentration and operating conditions on forward osmosis and pressure retarded osmosis performance in a spiral wound module. *Journal of Membrane Science*, 348(1–2), 298–309. <https://doi.org/10.1016/j.memsci.2009.11.013>
- Yip, N. Y., Tiraferri, A., Phillip, W. A., Schiffman, J. D., & Elimelech, M. (2010). High performance thin-film composite forward osmosis membrane. *Environmental Science and Technology*, 44(10), 3812–3818. <https://doi.org/10.1021/es1002555>